

NeurCADRecon: Neural Representation for Reconstructing CAD Surfaces by Enforcing Zero Gaussian Curvature

QIUJIE DONG, Shandong University, China
 RUI XU, Shandong University, China
 PENGFEI WANG, The University of Hong Kong, China
 SHUANGMIN CHEN, Qingdao University of Science and Technology, China
 SHIQING XIN*, Shandong University, China
 XIAOHONG JIA, AMSS, Chinese Academy Of Sciences, China
 WENPING WANG, Texas A&M University, USA
 CHANGHE TU, Shandong University, China

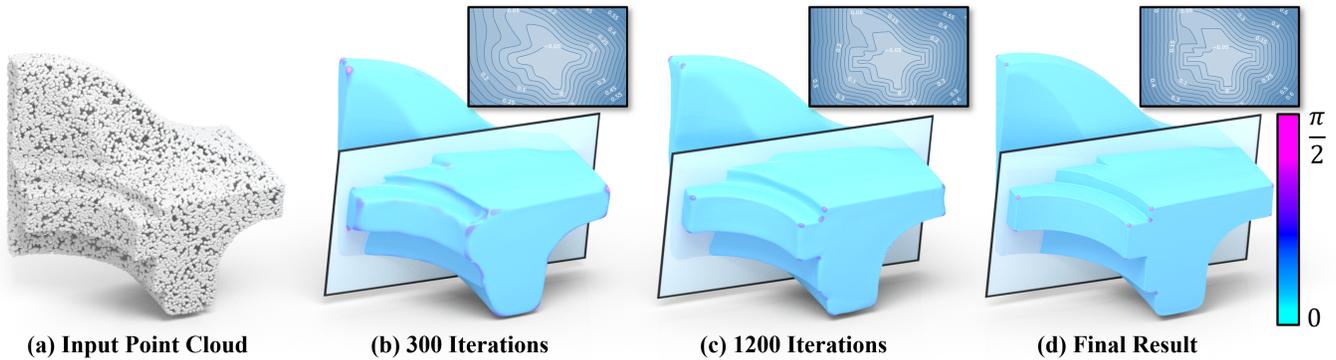


Fig. 1. In this paper, we propose a self-supervised deep neural network for reconstructing a CAD model from an unoriented point cloud. Considering that the surface of a CAD model is piecewise smooth, with each surface patch being approximately developable, we encourage the Gaussian curvature toward 0 while ensuring fidelity to the input points in the process of optimizing the signed distance function (see the close-up windows for the SDF visualization in a sectional plane). Tests on four public datasets show that our approach consistently outperforms the state-of-the-art methods, thanks to the utilization of the prior. From left to right: a point cloud with 10K points and the intermediate reconstruction results with color-coded visualization of absolute Gaussian curvatures (300 iterations, 1.2K iterations, and 9K iterations, respectively).

Despite recent advances in reconstructing an organic model with the neural signed distance function (SDF), the high-fidelity reconstruction of a CAD model directly from low-quality unoriented point clouds remains a significant challenge. In this paper, we address this challenge based on the prior observation that the surface of a CAD model is generally composed

of piecewise surface patches, each approximately developable even around the feature line. Our approach, named *NeurCADRecon*, is self-supervised, and its loss includes a developability term to encourage the Gaussian curvature toward 0 while ensuring fidelity to the input points (see the teaser figure). Noticing that the Gaussian curvature is non-zero at tip points, we introduce a double-trough curve to tolerate the existence of these tip points. Furthermore, we develop a dynamic sampling strategy to deal with situations where the given points are incomplete or too sparse. Since our resulting neural SDFs can clearly manifest sharp feature points/lines, one can easily extract the feature-aligned triangle mesh from the SDF and then decompose it into smooth surface patches, greatly reducing the difficulty of recovering the parametric CAD design. A comprehensive comparison with existing state-of-the-art methods shows the significant advantage of our approach in reconstructing faithful CAD shapes.

*Corresponding author: Shiqing Xin.

Authors' addresses: Qiujie Dong, Shandong University, Qingdao, Shandong, China, qiujie.jay.dong@gmail.com; Rui Xu, Shandong University, Qingdao, Shandong, China, xrvtid@163.com; Pengfei Wang, The University of Hong Kong, Hong Kong, China, pf.wang.graphics@qq.com; Shuangmin Chen, Qingdao University of Science and Technology, Qingdao, Shandong, China, csmqq@163.com; Shiqing Xin, Shandong University, Qingdao, Shandong, China, xinshiqing@sdu.edu.cn; Xiaohong Jia, AMSS, Chinese Academy Of Sciences, Beijing, China, xhjia@amss.ac.cn; Wenping Wang, Texas A&M University, Texas, USA, wenping@tamu.edu; Changhe Tu, Shandong University, Qingdao, Shandong, China, chtu@sdu.edu.cn.

Permission to make digital or hard copies of all or part of this work for personal or classroom use is granted without fee provided that copies are not made or distributed for profit or commercial advantage and that copies bear this notice and the full citation on the first page. Copyrights for components of this work owned by others than ACM must be honored. Abstracting with credit is permitted. To copy otherwise, or republish, to post on servers or to redistribute to lists, requires prior specific permission and/or a fee. Request permissions from permissions@acm.org.

© 2024 Association for Computing Machinery.

XXXX-XXXX/2024/4-ART \$15.00

<https://doi.org/10.1145/nnnnnnn.nnnnnnn>

CCS Concepts: • **Computing methodologies** → **Mesh models; Point-based models; Mesh geometry models.**

Additional Key Words and Phrases: CAD model, unoriented point cloud, surface reconstruction, signed distance function, Gaussian curvature

ACM Reference Format:

Qiujie Dong, Rui Xu, Pengfei Wang, Shuangmin Chen, Shiqing Xin, Xiaohong Jia, Wenping Wang, and Changhe Tu. 2024. NeurCADRecon: Neural Representation for Reconstructing CAD Surfaces by Enforcing Zero Gaussian Curvature. 1, 1 (April 2024), 17 pages. <https://doi.org/10.1145/nnnnnnn.nnnnnnn>

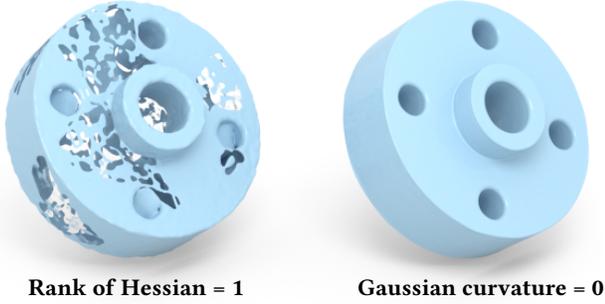


Fig. 2. Despite being mathematically correct, enforcing the rank of the Hessian matrix to be 1 may lead to numerical instability. In this paper, we propose to reconstruct CAD shapes by minimizing the overall absolute Gaussian curvature.

1 INTRODUCTION

Reverse engineering of CAD products is a fundamental yet challenging task with diverse applications in both academic and industrial communities [Yu et al. 2022]. While significant progress has been made in reconstructing an organic model directly from a low-quality unoriented point cloud [Gropp et al. 2020; Sitzmann et al. 2020; Wang et al. 2022b; Xu et al. 2022], the high-fidelity reconstruction of a CAD model remains a significant challenge. This challenge arises from the fact that the surface of a CAD model may contain sharp feature points/lines, posing a considerable obstacle when encoding the shape using a neural signed distance function (SDF).

The prominent characteristic of CAD models lies in that they are commonly piecewise, with each surface patch being smooth and approximately developable, which holds true even for a point on the feature line. Given that developability can be characterized by zero Gaussian curvature, it is reasonable to encourage the Gaussian curvature toward 0 in surface reconstruction, as illustrated in the inset figure depicting Gaussian curvature on the free model and CAD model. Based on this observation, we propose a self-supervised neural network to learn the signed distance function (SDF) of the underlying surface. In implementation, we inherit the Dirichlet condition [Lipman 2021] and the Eikonal condition [Gropp et al. 2020] to ensure fidelity while adding a loss term to minimize the overall absolute Gaussian curvature. With increasing iterations, the SDF can not only respect the input point cloud but also manifest the sharp feature points. See the teaser figure for an illustration.

Suppose that p is a surface point with a normal vector \mathbf{n}_p , where the two principal curvature directions are α_p and β_p with the corresponding principal curvatures being κ_1 and κ_2 , respectively. According to the well-established relationship between curvatures and the Hessian matrix of the SDF, \mathbf{n}_p , α_p , and β_p define the three eigenvectors of the Hessian matrix H with at least two zero eigenvalues, one of which corresponds to \mathbf{n}_p and the other corresponds to α_p or β_p . Because of this, a traditional formulation of zero Gaussian curvature



is achieved by enforcing the rank of H to be at most 1.0 [Sellán et al. 2020]. Despite its correctness in mathematics, it fails to consistently report a reasonable solution due to numerical instability; See Fig. 2 for the difference. We shall discuss this problem in Section 3.2.

In addition, the implementation process requires addressing at least three challenges. Firstly, as depicted in the teaser figure, the Gaussian curvature significantly deviates from 0 at tip points. Typical corner points display a Gaussian curvature of approximately $\pi/2$. Imposing a universal constraint of 0 may result in an undesirable bulge around the tip points. To address this, we introduce a double-trough curve to accommodate the presence of tip points. Secondly, considering that some CAD surfaces may have non-developable surface patches, we employ the technique of learning rate annealing to gradually reduce the influence of developability over time. Lastly, the input points may exhibit various imperfections, such as missing parts or high sparsity. If the loss is measured solely around the input point cloud, it is unlikely to enforce the constraints over the entire surface. Therefore, we implement a dynamic sampling strategy, enabling adaptive loss measurement that varies with changes in the underlying surface.

Our contributions are three-fold:

- (1) We propose to learn the neural SDF, in a self-supervised fashion, from a low-quality unoriented point cloud that potentially represents a CAD model, inspired by the fact that CAD model surfaces are typically piecewise smooth and approximately developable.
- (2) We define the developability loss term for encouraging the target Gaussian curvature to be either 0 or around $\pi/2$ (tolerating the existence of tip points), which is achieved by introducing a double-trough curve.
- (3) We leverage dynamic sampling to handle data imperfections, allowing for adaptive loss measurement varying with changes in the underlying surface. Extensive tests on four open datasets showcase our significant advantage in reconstructing CAD-type shapes; See Fig. 3 for a gallery of reconstruction results.

2 RELATED WORK

This paper focuses on reconstructing CAD-type point clouds within the surface reconstruction category. The section commences with a review of traditional reconstruction approaches, proceeds to explore deep learning-based methods, and concludes by addressing surface reconstruction under the assumption that the underlying surface represents a CAD model.

2.1 Traditional Approaches

Traditional implicit reconstruction approaches, extensively studied in computer graphics [Calakli and Taubin 2011; Kolluri 2008; Ohtake et al. 2003; Öztireli et al. 2009; Schroers et al. 2014; Shen et al. 2004; Xu et al. 2023], have played a significant role in this field. Carr et al. [2001] pioneered the use of radial basis functions (RBF) to fit the zero-isosurface of the Signed Distance Function (SDF), enabling the reconstruction of smooth surfaces. This approach saw later refinements by Huang et al. [2019] and Li et al. [2016]. Furthermore, Kazhdan et al. [2020; 2013; 2006] introduced Poisson surface reconstruction (PSR) and its subsequent variants, formulating the



Fig. 3. A gallery of reconstruction results by our NeurCADRecon. The central idea is to encourage the Gaussian curvature toward 0 while ensuring fidelity to the input points.

problem of computing the underlying occupancy field as a Poisson equation. However, PSR-based methods are limited to oriented points. To address this limitation, Hou et al. [2022] presented an improved PSR (iPSR) method, iteratively taking the normals obtained from the current reconstructed surface as input for the next iteration, completely eliminating the dependence on point normals. Parametric Gauss Reconstruction (PGR) [Lin et al. 2022] focuses more on the global consistency of normal orientations, building on the Gauss formula in potential theory to infer the occupancy field. However, none of the mentioned approaches are specifically designed for CAD-type point clouds.

2.2 Learning-Based Approaches

As with other learning-based tasks, implicit surface reconstruction methods encompass both supervised and self-supervised approaches.

Supervision Based. By leveraging prior information provided by ground-truth shape assemblies, supervision-based implicit surface reconstruction methods [Chabra et al. 2020; Erler et al. 2020; Jiang et al. 2020; Lin et al. 2023; Mescheder et al. 2019; Park et al. 2019; Tang et al. 2021b,a; Wang et al. 2022a] aim to learn the implicit representation (e.g., SDF or occupancy field) of the given point cloud. Peng et al. [2021] introduced a differentiable point-to-mesh layer using a differentiable formulation of Poisson Surface Reconstruction (PSR), enabling a GPU-accelerated fast solution for the indicator function. This concept was further extended by Huang et al. [2022] to incorporate learnable basis functions. Additionally, ConvONet [Peng et al. 2020] employed a convolutional architecture to map 3D points to a feature grid, initially designed for predicting occupancy fields. Furthermore, Bouch and Marlet [2022] enhanced the quality and performance of ConvONet [Peng et al. 2020] by replacing convolutions with a transformer architecture.

Self-supervision Based. Self-supervised implicit surface reconstruction methods [Ma et al. 2022; Zhou et al. 2022] are often referred

to as fitting-based methods. These approaches directly fit the implicit representation from raw point clouds without relying on any ground truth shape assemblies, thus enhancing their generalization capability. SAL [Atzmon and Lipman 2020, 2021] introduces Sign Agnostic Learning (SAL), characterized by a family of loss functions that can be applied directly to unsigned geometric data. This approach produces signed implicit representations of surfaces. IGR [Gropp et al. 2020] utilizes the Eikonal term to achieve implicit geometric regularization, offering an effective method for reconstructing surfaces. SIREN [Sitzmann et al. 2020] achieves impressive reconstruction results by utilizing periodic activation functions. These functions preserve high frequencies while maintaining low-frequency implicit representations through the bias of ReLU-MLPs. Inspired by SIREN, Wang et al. [2021] proposed a hybrid neural surface representation. This method focuses on imposing geometry-aware sampling and regularization, using iso-points as an explicit representation for a neural implicit function. Neural-Pull [Ma et al. 2021] advocates for predicting both the signed distance and gradients simultaneously. This allows a query point to be pulled to the nearest point on the underlying surface, enhancing accuracy. DiGS [Ben-Shabat et al. 2022] applies the Laplacian energy as a soft constraint of the Signed Distance Function (SDF). This method is effective for reconstructing surfaces from unoriented point clouds. Lastly, Neural-Singular-Hessian [Wang et al. 2023] enforces the Hessian of the neural implicit function to have a zero determinant for points near the surface. This approach is particularly useful for recovering details from unoriented point clouds.

2.3 Surface Reconstruction of CAD Models

In addressing the challenge of reconstructing CAD-type models, there has been significant prior research, notably by Sharma et al. [2018] and Kania et al. [2020], focusing on primitive fitting. Li et al. [2019] employed supervised learning to initially detect primitive types and fit various primitive patches, including planes, cylinders, cones, and spheres. Sharma et al. [2020] extended SPFN's approach by incorporating B-spline patches and integrating differentiable

metric-learning segmentation, representing a step forward in the field. Uy et al. [2021] segmented raw 3D point clouds into sets of extrusion cylinders, using boolean combination operations to merge these primitives, presenting a novel approach to the problem. Yu et al. [2022] introduced an unsupervised approach that similarly involved primitive prediction and boolean combination operations. However, both of the approaches [Uy et al. 2021; Yu et al. 2022] favor voxelized inputs over point clouds. This necessitates the voxelization of oriented point clouds before they are input into the neural network, or before being used to learn a latent code.

It is evident that directly using specific primitives to fit a complex CAD model from a low-quality point cloud may not be practical. Therefore, we propose an alternative: fitting a high-fidelity neural Signed Distance Function (SDF) that can clearly manifest distinct feature points and lines. With a geometry that is sufficiently faithful, it becomes straightforward to discretize it into a set of surface patches and recover the parametric design. For an illustrative example, see Section 4.2.

3 OUR APPROACH

As with other existing self-supervision based methods, our approach, named *NeurCADRecon*, takes an unoriented point cloud as input and focuses on learning the neural Signed Distance Function (SDF) to accurately represent the underlying surface. The design of *NeurCADRecon* is centered around two key aspects. Firstly, it inherits the Dirichlet condition [Lipman 2021] and the Eikonal condition [Gropp et al. 2020] to ensure high fidelity to the input points. Secondly, *NeurCADRecon* emphasizes encouraging the Gaussian curvature towards zero, which is crucial for highlighting the sharp features characteristic of CAD models.

3.1 Preliminaries

We assume that the input is a point cloud, \mathcal{P} , which does not include normals. The goal is to predict a neural Signed Distance Function (SDF), denoted as $f(\mathbf{x}; \Theta) : \mathbb{R}^3 \rightarrow \mathbb{R}$, such that its zero level-set accurately represents the underlying surface, \mathcal{S} . Here, Θ symbolizes the computational parameters of a network that necessitate frequent optimization and updates.

Despite their differences, existing approaches primarily concentrate on developing a geometrically meaningful loss function to aid in discovering the desired solution. Given that $\mathbf{p} \in \mathcal{P}$ is considered to be on the surface \mathcal{S} , it is often labeled as a manifold point. Moreover, a distinct set of sample points, \mathcal{Q} , usually uniformly sampled from its bounding box (normalized to the range $[-0.5, 0.5]^3$ by default), is employed to help regularize the characteristics of the underlying SDF. In the following, we provide a brief overview of the Dirichlet condition and the Eikonal condition. These conditions have been extensively discussed in the research community and have proven to be valuable in works such as Gropp et al. [2020], Sitzmann et al. [2020], Atzmon and Lipman [2020], Ma et al. [2021], and Ben-Shabat et al. [2022].

Eikonal Condition. As a valid SDF, $f(\mathbf{x}; \Theta)$ must possess a unit gradient for each point $\mathbf{p} \in \mathcal{P}$, i.e., that is $\|\nabla_{\mathbf{p}} f\| = 1$. Based on this

requirement, the Eikonal condition can be written as a loss term:

$$\mathcal{L}_E = \frac{1}{|\mathcal{P}| + |\mathcal{Q}|} \int_{\mathcal{P} \cup \mathcal{Q}} |1 - \|\nabla f(\mathbf{x}; \Theta)\|| d\mathbf{x}, \quad (1)$$

where $|\cdot|$ is the operator for taking the number of elements.

Dirichlet Condition. For any point \mathbf{p} within \mathcal{P} , it is crucial that they align closely with the reconstructed surface, ideally satisfying $f(\mathbf{p}; \Theta) = 0$ as much as possible. This alignment ensures that the points from the input cloud are accurately represented on the surface. Conversely, for any point \mathbf{q} in \mathcal{Q} , we regard it as external to the underlying surface, hence we encourage $f(\mathbf{q}; \Theta) \neq 0$. This helps regularize the shape by delineating the surface from the surrounding space. They can be respectively written as loss terms:

$$\mathcal{L}_{DM} = \frac{1}{|\mathcal{P}|} \int_{\mathcal{P}} |f(\mathbf{p}; \Theta)| d\mathbf{p}, \quad (2)$$

and

$$\mathcal{L}_{DNM} = \frac{1}{|\mathcal{Q}|} \int_{\mathcal{Q}} \exp(-\alpha |f(\mathbf{q}; \Theta)|) d\mathbf{q}. \quad (3)$$

Given that the input point cloud lacks normals, there is no need to impose constraints on normal vectors. In light of this, the loss function comprises three terms as below:

$$\mathcal{L}_{\text{basic}} = \lambda_E \mathcal{L}_E + \lambda_{DM} \mathcal{L}_{DM} + \lambda_{DNM} \mathcal{L}_{DNM}. \quad (4)$$

However, $\mathcal{L}_{\text{basic}}$ fails to adequately capture the sharp feature points and lines that are typically associated with CAD geometries. This limitation underscores the need for integrating additional components into the loss function, aimed at enhancing the reconstruction fidelity of CAD models.

3.2 Gaussian Curvature Constraint Term

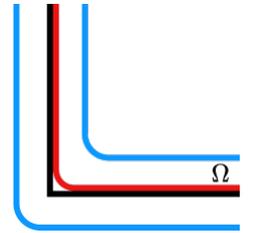
We observe that the surface of a CAD model is commonly piecewise smooth and approximately developable. Given that developability implies zero Gaussian curvature, we introduce an additional loss term to specify this requirement. The proposed loss term is formulated as follows:

$$\mathcal{L}_{\text{Gauss}}^{(1)} = \frac{1}{|\mathcal{P}|} \int_{\mathcal{P}} |k_{\text{Gauss}}(\mathbf{x})| d\mathbf{x}. \quad (5)$$

Recall that $f(\mathbf{x}; \Theta)$ aims to approximate the actual SDF and demonstrates differentiability throughout the entire space. Suppose we aim to reconstruct a target surface resembling the cube model depicted in the inset figure. The real SDF might not be differentiable within a sufficiently narrow space surrounding the original surface due to sharp feature lines.

However, by slightly smoothing these sharp feature lines, we can establish a narrow differential space Ω . This adjustment allows us to leverage the differential properties of $f(\mathbf{x}; \Theta)$ to estimate various geometric quantities effectively.

For example, for a point $\mathbf{x} \in \Omega$, the Gaussian curvature of \mathbf{x} can be estimated through the hessian $H_f(\mathbf{x})$ [Goldman 2005; Knoblauch



1913; Spivak 1975]:

$$k_{\text{Gauss}}(\mathbf{x}) = -\frac{\begin{vmatrix} H_f(\mathbf{x}) & \nabla f^T(\mathbf{x}; \Theta) \\ \nabla f(\mathbf{x}; \Theta) & 0 \end{vmatrix}}{\|\nabla f(\mathbf{x}; \Theta)\|^4}. \quad (6)$$

Comparison with Rank Constraint. Suppose p is a surface point with a normal vector \mathbf{n}_p , and the two principal curvature directions at p are α_p and β_p , with the corresponding principal curvatures being κ_1 and κ_2 , respectively. The eigenvectors of the Hessian matrix H are represented by \mathbf{n}_p , α_p , and β_p . Firstly, the eigenvalue corresponding to \mathbf{n}_p is 0 [Wang et al. 2023]. Secondly, one of κ_1 and κ_2 must be 0 due to zero Gaussian curvature, i.e., $\kappa_1 \times \kappa_2 = 0$. This indicates that the rank of H_f is at most 1, as discussed in [Sellán et al. 2020]. Such a rank constraint has been utilized in achieving developability and fitting algebraic spline surfaces.

Despite the mathematical equivalence, the constraint of the rank being at most 1 faces numerical challenges. Firstly, a slight change in H_f can cause a jump in the rank, hinting at potential numerical instability. Secondly, when the target shape resembles a cube-like model, the neural SDF f cannot exactly match the actual SDF, as the latter is not differentiable even in a very narrow space around the surface. The neural SDF f , despite being slightly from the actual SDF, has a narrow space Ω surrounding the surface. Although it is convenient to estimate Gaussian curvature through the neural SDF f (slightly from the actual SDF) and its Hessian matrix H_f , the rank of H_f may not reflect the real situation. Therefore, in this paper, we propose minimizing the overall absolute Gaussian curvature to achieve the goal of developability.

Sampling Strategy for Representing Ω . Clearly, it is unfeasible to consider the contribution of every point in Ω directly. Following the practices of works like Gropp et al. [2020], Ma et al. [2021], and Zhou et al. [2022], we utilize a sampling strategy that involves Gaussian distributions centered on each input point $\mathbf{p} \in \mathcal{P}$ to select points from Ω . To elaborate, for a given point $\mathbf{p} \in \mathcal{P}$, the Gaussian distribution is centered at \mathbf{p} , with its mean and standard deviation determined by the distance to its k -th nearest neighbor, where k is set to 50 by default. This method employs a one-point sampling technique for each distribution to maintain a consistent number of points sampled from Ω (15K by default) aligning with the batch size used in training. By abusing notations, we reformulate the Gaussian curvature term as follows:

$$\mathcal{L}_{\text{Gauss}}^{(2)} = \frac{1}{|\Omega|} \int_{\Omega} |k_{\text{Gauss}}(\mathbf{x})| d\mathbf{x}. \quad (7)$$

3.3 Double-trough Function

As illustrated in Fig. 4(a), it is clear that the Gaussian curvature at tip points is non-zero, a characteristic frequently observed in many CAD models. Moreover, the Gaussian curvature at a tip point significantly deviates from 0, typically approaching a value around $\pi/2$. Consequently, we need to tolerate the existence of non-zero Gaussian curvature at the tip points while leaning towards encouraging a Gaussian curvature closer to 0. For such a purpose, we invent a double-trough function, as is shown in Fig. 4(b).

The key idea involves mapping the Gaussian curvature of around $\pi/2$ to a value close to 0. To achieve this, we define the double-trough

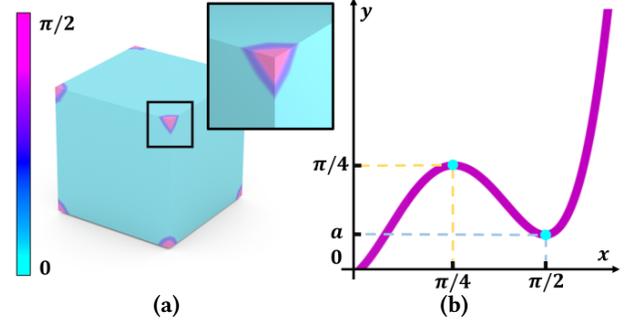


Fig. 4. (a) The Gaussian curvature field on the cube model shows significant deviations from 0 at the tip points. (b) To accommodate the non-zero Gaussian curvature at the tip points, we advocate the use of a double-trough function. This function is designed to permit the desired Gaussian curvature to assume values of either 0 or approximately $\pi/2$.

curve $\text{DT}(t)$ based on the following requirements:

$$\begin{cases} \text{DT}(0) = 0 \\ \text{DT}(\pi/4) = \pi/4 \\ \text{DT}'(\pi/4) = 0 \\ \text{DT}(\pi/2) = a \\ \text{DT}'(\pi/2) = 0. \end{cases} \quad (8)$$

We explain the equations as follows. $\text{DT}'(\pi/4) = 0$ is used to form a peak at $\pi/4$ while $\text{DT}'(\pi/2) = 0$ is used to form a valley at $\pi/2$, with a height of a . We set a to 1/4 by default, indicating that while the presence of non-zero Gaussian curvature is allowed, it is more inclined to favor zero Gaussian curvature. It is easy to find a quartic function to satisfy the four equations at the same time:

$$\text{DT}(t) = \frac{64\pi - 80}{\pi^4} t^4 - \frac{64\pi - 88}{\pi^3} t^3 + \frac{16\pi - 29}{\pi^2} t^2 + \frac{3}{\pi} t. \quad (9)$$

To this end, we can reformulate the Gaussian curvature term as follows:

$$\mathcal{L}_{\text{Gauss}} = \frac{1}{|\Omega|} \int_{\Omega} \text{DT}(|k_{\text{Gauss}}(\mathbf{x})|) d\mathbf{x}. \quad (10)$$

In Fig. 5, we showcase the effectiveness of the double-trough curve. It can be seen that, in the absence of the tolerating technique, bulges are prone to form around the tip points. Furthermore, with regard to reconstruction accuracy, the application of the double-trough technique results in enhanced accuracy. This improvement is represented through the color-coded visualization of the Hausdorff distance between the reconstructed polygonal surface and the ground truth, underscoring the benefits of the double-trough approach in better representing the SDF of CAD-type models.

3.4 Implementation Details

Annealing Factor. To this end, our total loss is like the following:

$$\mathcal{L} = \lambda_E \mathcal{L}_E + \lambda_{\text{DM}} \mathcal{L}_{\text{DM}} + \lambda_{\text{DNM}} \mathcal{L}_{\text{DNM}} + \tau \lambda_{\text{Gauss}} \mathcal{L}_{\text{Gauss}}, \quad (11)$$

where τ is the annealing factor, which is used to gradually reduce the influence of the Gaussian curvature. The annealing process is detailed in Section 4.1. In Fig. 6(a), we illustrate the iterative process using a sphere-shaped point cloud comprising 10K points as

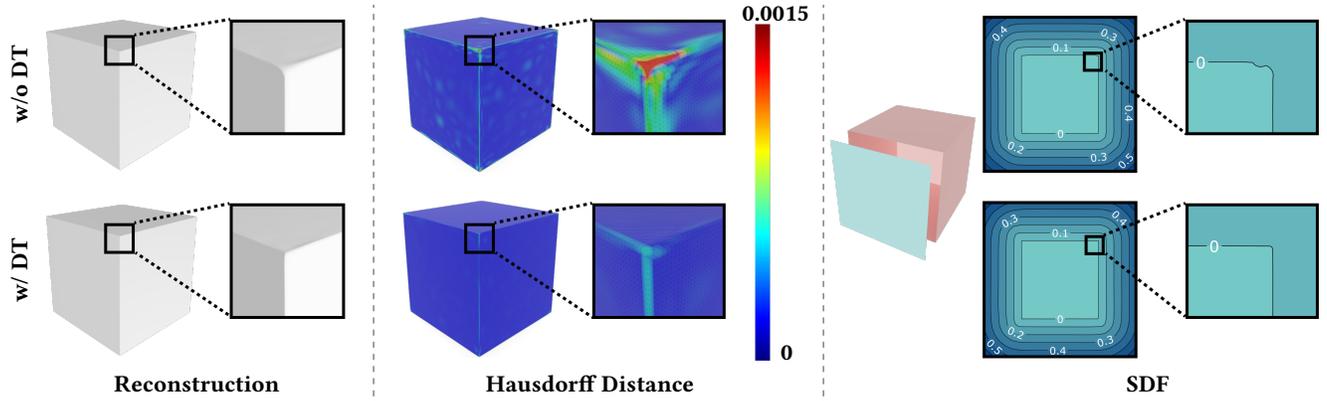


Fig. 5. By utilizing a specially designed double-trough (DT) curve, we allow the presence of non-zero Gaussian curvature, but are more inclined to favor zero Gaussian curvature. Without the usage of the tolerating technique, bulges may arise around the tip points.

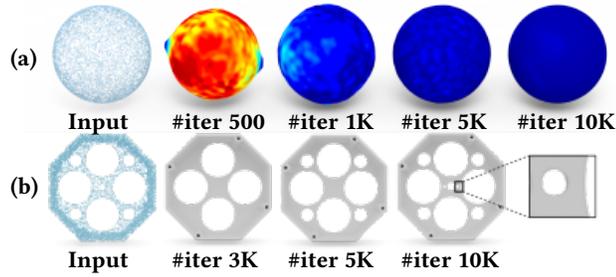


Fig. 6. We use an annealing factor to gradually reduce the influence of the Gaussian curvature, such that the fidelity can be preserved even for (a) non-developable surfaces and (b) tiny structures.

input. It is important to note that for a sphere model, the Gaussian curvature cannot be zero for points on the surface. Owing to the implementation of an annealing factor, our Gaussian curvature loss term gradually diminishes throughout the fitting process, ultimately resulting in a high-fidelity representation of the sphere model. In practice, a CAD model may contain multiple feature parts at significantly different scales. By leveraging the annealing factor, our method demonstrates the capability to reconstruct structures of varying sizes. In Fig. 6(b), the model includes tiny structures as small as 0.03 in size, within a total size range of $[-0.5, 0.5]^3$. Nonetheless, our algorithm is still able to recover these tiny structures effectively.

Dynamic Sampling. In the presence of data imperfections in the given point cloud, such as high sparsity and missing parts, the point set Ω , around the original point set \mathcal{P} , may prevent the loss term $\mathcal{L}_{\text{Gauss}}$ from being evaluated in the missing parts. To address this issue, additional sample points are required near the current surface, enabling $\mathcal{L}_{\text{Gauss}}$ to more effectively guide the surface’s evolution, especially in areas lacking data.

This dynamic sampling process involves projecting each point Q onto the current surface. For each point $x \in Q$, the projection x' is calculated as (see Fig. 7):

$$x' = x - \frac{\nabla f(x; \Theta)}{\|\nabla f(x; \Theta)\|} \cdot f(x; \Theta). \quad (12)$$

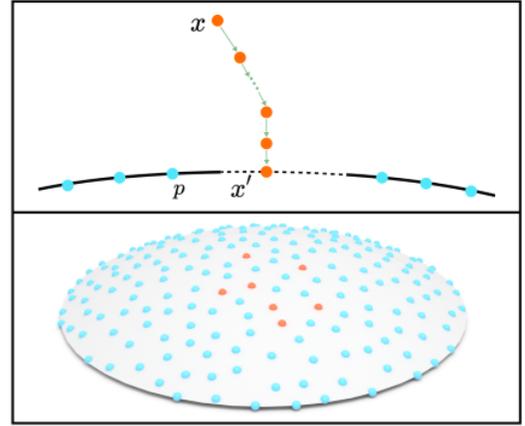


Fig. 7. We project a point onto the surface based on Eq. (12). The projection points are colored in orange.

Subsequently, $\mathcal{L}_{\text{Gauss}}$ is evaluated for the points in $\Omega \cup Q'$. As the surface undergoes updates, the set Q' is updated accordingly.

Without dynamic sampling, the Gaussian curvature term cannot be enforced within the data-missing parts. In this case, existing approaches fill the missing parts with a smooth transition. In this paper, by employing the technique of dynamic sampling to address data imperfections, we generate additional sample points in close proximity to the current surface, thereby enabling the loss function to more effectively influence the surface’s evolution, particularly in areas where data may be missing. As Fig. 8 shows, it is evident that despite the presence of data imperfections across feature points and lines, our algorithm is capable of accurately recovering these actual sharp feature points and lines.

4 EXPERIMENTS

In this section, we begin by detailing the implementation specifics and clarifying the metrics employed for evaluation. Following this, a thorough assessment of our NeurCADRecon is carried out across several datasets. Finally, we illustrate its effectiveness in modeling

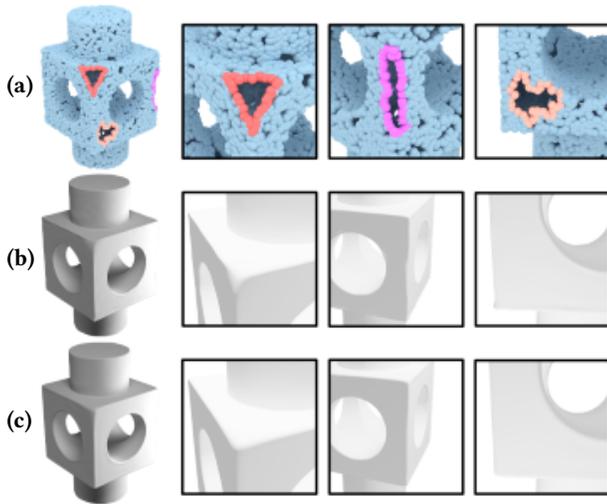


Fig. 8. In the presence of data imperfections across feature points and lines (a), a fixed sampling point set can effectively enforce the Gaussian curve constraints over the surface, particularly within the missing parts (b). We employ the technique of dynamic sampling to address data imperfections, thereby effectively influencing the surface’s evolution, particularly in areas where data may be missing. It is evident that despite the presence of data imperfections across feature points and lines, our algorithm is capable of accurately recovering these actual sharp feature points and lines (c).

developable surfaces and its competency in handling a range of data imperfections.

4.1 Experimental Setting

Parameters and Platform. Similar to various implicit surface reconstruction methods [Ben-Shabat et al. 2022; Lipman 2021; Wang et al. 2022b], our NeurCADRecon employs the SIREN [Sitzmann et al. 2020] network architecture, featuring four hidden layers, each with 256 units. The SIREN [Sitzmann et al. 2020] architecture comprises layers based on MLPs, with inputs initially normalized to the range $[-1, 1]^3$ before being fed into the network. The activation function employed in this method is the sine periodic function. In our experiments, we determine the weights ($\lambda_E = 50, \lambda_{DM} = 7000, \lambda_{DNM} = 600, \lambda_{Gauss} = 10$) based on our tailored configurations. The annealing factor τ remains at 1 during the initial 20% of iterations, then linearly decreases to 1×10^{-4} from 20% to 50% of the iteration span, and finally drops to 0 towards the end. We extract the zero-level set of the implicit function into a discrete mesh using the marching cubes algorithm [Lewiner et al. 2003] with a 256^3 grid. Throughout the training phase, we apply the Adam optimizer [Kingma and Ba 2014] with a default learning rate of 5×10^{-5} and complete 10K iterations. The experiments detailed in this paper were executed on an NVIDIA GeForce RTX 3090 graphics card equipped with 24GB of video memory and powered by an AMD EPYC 7642 processor.

Evaluation Metrics. To evaluate the accuracy of the reconstructed mesh, we utilize three primary metrics: Chamfer Distance (CD), F1-score (F1), and Normal Consistency (NC). CD, scaled by 10^3 and calculated using the $L1$ -norm, quantifies the similarity between

two surfaces. F1, scaled by 10^2 and employing a default threshold of 5×10^{-3} , represents the harmonic mean of precision and recall, assessing the balance between the detail capture and the inclusion of extraneous elements. NC, also scaled by 10^2 , measures the agreement between the normals of the reconstructed surface and those of the ground-truth, indicating the directional accuracy of the surface details. The mean values along with the standard deviation of the reconstruction outcomes across each dataset are documented to provide a comprehensive overview of the performance.

Datasets. We carry out overfitting surface reconstruction experiments on four recent CAD datasets: ABC [Koch et al. 2019], Fusion Gallery [Willis et al. 2021], DeepCAD [Wu et al. 2021], and the dataset utilized by CAPRI-Net [Yu et al. 2022]. To maintain uniformity in evaluation, all meshes are scaled to fit within the range of $[-0.5, 0.5]^3$, and 10K points are sampled from each mesh, ensuring a consistent and fair basis for comparison across all datasets.

4.2 Comparison on Open Datasets

We evaluate our proposed method, NeurCADRecon, against three categories of state-of-the-art surface reconstruction techniques:

- **Approaches with Normals:** In this category, we include the classic surface reconstruction method SPSR [Kazhdan and Hoppe 2013] for comparison, which utilizes normals in its process.
- **Supervision-based Approaches:** This category comprises two methods, POCO [Boulch and Marlet 2022] and Neural Galerkin (NG) [Huang et al. 2022], both of which depend on ground truth data for training. To enhance the performance of POCO and NG, we retrained these methods on the comprehensive ShapeNet dataset [Chang et al. 2015] using 10K input points prior to comparing them with our approach.
- **Overfitting-based Approaches:** Methods in this category leverage various reconstruction loss constraints for self-supervised learning, including DiGS [Ben-Shabat et al. 2022], SIREN [Sitzmann et al. 2020], Neural-Pull [Ma et al. 2021], IGR [Gropp et al. 2020], SAL [Atzmon and Lipman 2020], CAPRI-Net [Yu et al. 2022], iPSR [Hou et al. 2022], NSH [Wang et al. 2023], and our own NeurCADRecon. It’s noteworthy that CAPRI-Net [Yu et al. 2022] operates in two phases: pre-training and fine-tuning, with a detailed comparison provided in Subsection 4.2.

In Fig. 9, we showcase a variety of challenging CAD models, such as thin tubes, tiny links, sharp corners, and narrow slits, to qualitatively demonstrate that our results are capable of handling complex CAD geometries in comparison with the aforementioned methods.

ABC Dataset. The ABC dataset, as described in Koch et al. [2019], comprises a diverse assortment of CAD meshes. Following the approach of Erler et al. [2020], we select 100 [Erler et al. 2020; Ma et al. 2021; Wang et al. 2023] mechanically intricate yet clean and watertight shapes from the dataset and randomly sample 10K or 5K points from each mesh. In Tab. 1, quantitative comparison statistics between our method and the baseline approaches are presented. Our method demonstrates superior performance across all three

Table 1. Quantitative comparison on the ABC dataset [Koch et al. 2019]. Each raw point cloud has 10K or 5K points. Methods denoted with a ‘*’ necessitate point normals for their operation, and those marked with ‘+’ rely on supervision-based training. Within each column, the best scores are emphasized with bold and underlining (**best**), whereas the second-best scores are simply highlighted in bold (**second best**).

	10K Points						5K Points					
	NC \uparrow		CD \downarrow		F1 \uparrow		NC \uparrow		CD \downarrow		F1 \uparrow	
	mean	std.	mean	std.	mean	std.	mean	std.	mean	std.	mean	std.
SPSR* [Kazhdan and Hoppe 2013]	95.16	4.48	4.39	3.05	74.54	26.65	93.06	6.31	6.36	6.55	62.91	30.07
SAL [Atzmon and Lipman 2020]	86.25	8.39	17.30	14.82	29.60	18.04	83.85	11.28	23.78	30.48	28.61	18.99
IGR [Gropp et al. 2020]	82.14	16.12	36.51	40.68	43.47	40.06	81.29	17.97	37.44	41.37	41.14	37.57
SIREN [Sitzmann et al. 2020]	82.26	9.24	17.56	15.25	30.95	22.23	81.75	10.45	18.76	19.71	22.02	26.92
Neural-Pull [Ma et al. 2021]	94.23	4.57	6.73	5.15	42.67	10.75	92.52	8.51	6.97	10.37	72.32	27.74
DiGS [Ben-Shabat et al. 2022]	94.48	6.12	6.91	6.94	66.22	32.01	92.55	7.11	7.91	6.96	55.86	31.52
iPSR [Hou et al. 2022]	93.15	7.47	4.84	4.06	71.59	24.96	90.57	8.71	6.21	4.49	61.27	26.23
PGR [Lin et al. 2022]	94.11	4.63	4.52	2.13	68.91	27.86	89.29	7.91	7.96	3.76	43.27	23.12
POCO+ [Boulch and Marlet 2022]	92.90	7.00	6.05	6.80	68.29	26.05	90.24	5.71	7.93	5.07	48.25	23.89
NG+ [Huang et al. 2022]	95.88	3.88	3.60	1.38	81.38	20.39	94.07	5.31	4.05	1.71	76.42	21.03
NSH [Wang et al. 2023]	97.42	2.37	3.27	1.78	88.62	13.87	94.81	3.57	3.97	1.18	78.86	17.15
Ours	97.57	2.01	3.12	1.41	89.03	13.05	96.29	3.55	3.47	1.46	85.34	15.17

Table 2. Quantitative comparison on the Fusion Gallery dataset [Willis et al. 2021]. Each raw point cloud has 10K points.

	NC \uparrow		CD \downarrow		F1 \uparrow	
	mean	std.	mean	std.	mean	std.
SPSR* [Kazhdan and Hoppe 2013]	97.33	3.35	3.01	2.48	88.51	18.61
SAL [Atzmon and Lipman 2020]	92.42	7.58	13.31	21.98	47.16	28.45
IGR [Gropp et al. 2020]	87.07	14.71	29.75	37.73	54.09	42.67
SIREN [Sitzmann et al. 2020]	95.31	5.22	6.38	13.45	80.85	22.28
Neural-Pull [Ma et al. 2021]	98.05	3.25	3.93	7.26	89.99	20.51
DiGS [Ben-Shabat et al. 2022]	97.53	3.01	4.96	6.62	80.77	29.28
iPSR [Hou et al. 2022]	96.05	7.36	3.16	2.65	86.48	19.48
PGR [Lin et al. 2022]	93.55	8.19	4.84	3.13	67.52	26.36
POCO+ [Boulch and Marlet 2022]	94.63	3.45	6.91	7.04	69.31	28.08
NG+ [Huang et al. 2022]	97.87	2.79	2.68	1.29	90.78	15.11
NSH [Wang et al. 2023]	98.99	4.79	3.12	1.71	90.92	11.25
Ours	98.07	2.39	2.75	1.69	92.99	10.01

evaluation metrics, whether applied to input point clouds with 10K or 5K points. Notably, when reconstructing CAD models with only 5K input points, our F1 surpasses that of the second-best method by 6.48%. Then, we show the results of the reconstruction using varying points (5K and 10K) on one model (see the first model in Fig. 9). In visualization comparison with NSH [Wang et al. 2023], our method successfully reconstructs the thin tube structure in its entirety. In addition, our reconstruction results do not have redundant faces like the other methods.

Fusion Gallery Dataset. The Fusion Gallery dataset, as described in Willis et al. [2021], consists of 8625 human-designed CAD models generated using profile sketches and extrusions, with all CAD models derived from real-world application scenarios. In the analysis presented in this paper, we randomly selected 10K points from each mesh and input them to all approaches for comparison. Quantitative comparison statistics are provided in Tab. 2. The statistics indicate

Table 3. Quantitative comparison on the DeepCAD dataset [Wu et al. 2021]. Each raw point cloud has 10K points.

	NC \uparrow		CD \downarrow		F1 \uparrow	
	mean	std.	mean	std.	mean	std.
SPSR* [Kazhdan and Hoppe 2013]	97.73	2.47	3.12	3.91	87.43	19.74
SAL [Atzmon and Lipman 2020]	93.64	7.11	11.48	17.27	45.64	27.83
IGR [Gropp et al. 2020]	89.73	13.26	27.18	37.25	59.99	41.57
SIREN [Sitzmann et al. 2020]	94.77	6.46	8.79	20.27	76.16	25.91
Neural-Pull [Ma et al. 2021]	97.41	4.36	4.81	11.34	86.87	21.64
DiGS [Ben-Shabat et al. 2022]	97.74	2.39	5.24	6.84	77.93	31.12
iPSR [Hou et al. 2022]	96.99	4.84	3.25	2.66	85.29	20.25
PGR [Lin et al. 2022]	94.85	5.51	4.73	2.66	67.26	25.91
POCO+ [Boulch and Marlet 2022]	94.62	2.89	8.48	8.41	65.66	28.86
NG+ [Huang et al. 2022]	98.18	2.12	3.01	2.12	88.36	17.17
NSH [Wang et al. 2023]	97.98	2.38	3.15	2.39	87.63	24.16
Ours	98.03	2.17	3.08	2.26	90.70	12.82

that our method consistently achieves optimal results on average, demonstrating that the CAD models reconstructed by our method closely align with those designed by humans. In the comparison with tiny links (the second model in Fig.9), SAL [Atzmon and Lipman 2020], PGR [Lin et al. 2022], and POCO [Boulch and Marlet 2022] lose the part. Other methods create uneven surfaces, leading to the loss of feature lines. In contrast, our method successfully reconstructs this structure while maintaining the feature line.

DeepCAD Dataset. The DeepCAD dataset, detailed in Wu et al. [2021], comprises 178,238 CAD models created via sketch-extrude operations. In contrast to the Fusion Gallery Dataset [Willis et al. 2021], this dataset contains more CAD models with sharp features, such as sharp corners. In Tab. 3, we present the reconstruction results on the DeepCAD dataset, with all methods randomly sampling 10K points as input. Quantitatively, our method performs consistently with NG [Huang et al. 2022] on NC and CD, but we outperform

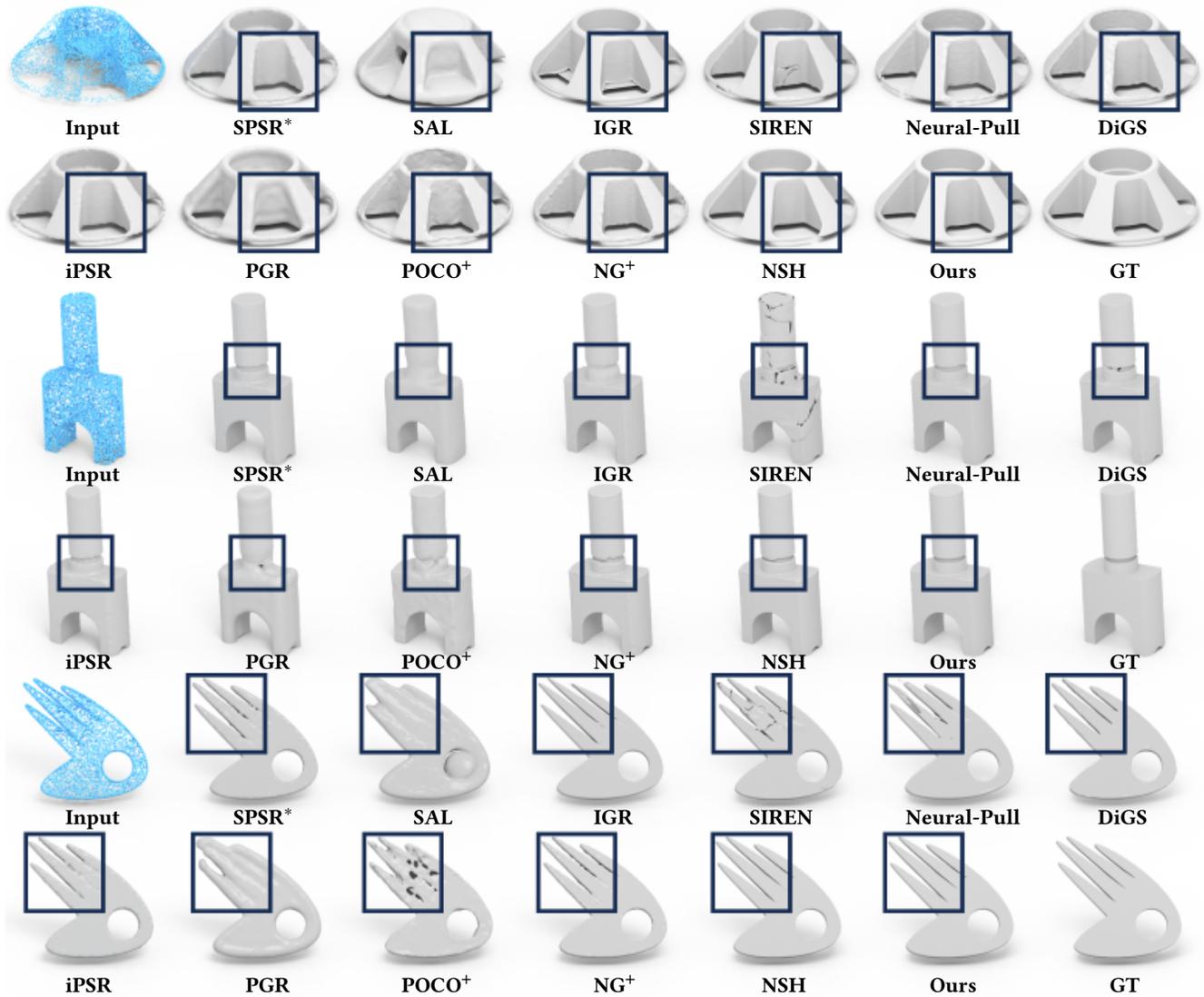


Fig. 9. Comparison with state-of-the-art surface reconstruction methods is conducted on a variety of challenging CAD models, including those with thin tubes, tiny links, sharp corners, and narrow slits. The first model showcases reconstruction results of varying density input points (10K and 5K simultaneously), while the remaining two models are based on 10K input points. Method marked with “*” requires normals, and those marked with “+” are supervision-based. Across the board, our NeurCADRecon outperforms other methods in terms of reconstruction fidelity on complex CAD models.

it by 1.8% on F1. The visual comparison results of sharp corners and narrow slits can be observed in the third model of Fig. 9. From the visualization, although many methods can reconstruct sharp corners, only our method and NSH [Wang et al. 2023] accurately reconstruct narrow slits close to the ground truth.

CAD Dataset from CAPRI-Net. The dataset utilized by CAPRI-Net [Yu et al. 2022] includes CAD models from ABC [Koch et al. 2019], where each model consists of complex components (as shown in Fig.3) and is provided in both point cloud and voxel forms. In this comparison, we input voxels to CAPRI-Net [Yu et al. 2022], while other methods take a point cloud with randomly sampled 10K points as input. Tab. 4 presents the quantitative comparison results between our method and other methods, excluding CAPRI-Net [Yu

et al. 2022]. We achieved optimal results across all three evaluation metrics.

To perform a comprehensive comparison with CAPRI-Net [Yu et al. 2022], we utilized the publicly available data and network weights of this method without re-training. Tab. 5 lists the quantitative results of CAPRI-Net [Yu et al. 2022] in both with and without fine-tuning phase, and Fig. 10 displays the corresponding reconstruction results. Our method consistently outperforms CAPRI-Net [Yu et al. 2022] in both quantitative and qualitative aspects. It is worth noting that CAPRI-Net [Yu et al. 2022] may encounter alignment issues with different predicted primitives during Boolean combination operations, leading to reconstruction results with redundant faces.

Table 4. Quantitative comparison on the CAPRI-Net [Yu et al. 2022] dataset. Each raw point cloud has 10K points.

	NC \uparrow		CD \downarrow		F1 \uparrow	
	mean	std.	mean	std.	mean	std.
SPSR* [Kazhdan and Hoppe 2013]	97.56	1.41	3.11	1.39	86.59	17.09
SAL [Atzmon and Lipman 2020]	92.71	5.38	10.88	8.52	44.29	22.43
IGR [Gropp et al. 2020]	91.36	12.22	10.55	14.12	67.07	30.93
SIREN [Sitzmann et al. 2020]	95.07	5.59	8.28	18.28	76.27	24.58
Neural-Pull [Ma et al. 2021]	97.02	5.89	6.23	18.02	86.44	21.83
DiGS [Ben-Shabat et al. 2022]	96.43	4.24	7.44	8.93	70.29	35.43
iPSR [Hou et al. 2022]	96.97	2.36	3.34	1.69	83.86	18.37
PGR [Lin et al. 2022]	94.26	3.77	5.18	2.07	60.37	22.76
POCO+ [Boulch and Marlet 2022]	93.76	3.36	7.07	5.72	61.18	26.22
NG ⁺ [Huang et al. 2022]	98.15	1.34	2.93	1.06	89.01	15.01
NSH [Wang et al. 2023]	97.48	1.47	4.21	3.88	85.81	15.53
Ours	98.42	1.10	2.84	1.36	92.79	9.64

4.3 Imperfection Data and Further Comparison

Noise. To evaluate the robustness of our method against noise, we introduced point clouds with reconstruction noise. We specifically used a 10K point cloud as the baseline input and added 0.5% Gaussian noise to test the noise immunity of our network. For a comprehensive comparison, we input the same point cloud to the other 11 methods under identical noise conditions. As depicted in Fig. 11, our approach outperforms the alternative methods in the noisy scenarios, which validates that our method can reconstruct faithful CAD models with smooth surfaces. The scalability of our method plays a significant role in its superior smoothing performance, which is instrumental in its effective resistance to noise. A more detailed comparison of our method with other smoothing functions is provided in Section 5.2.

Data Sparsity. In Fig. 12, we present an example with a sparse point cloud containing 1K points. This specific case is designed to assess the algorithm’s performance on sparse inputs, as nearby gaps and thin-walled tubes/plates can significantly increase the difficulty of predicting SDFs in situations of data sparsity. The visual comparison highlights that only our method, SIREN [Sitzmann et al. 2020], and NSH [Wang et al. 2023] successfully reconstruct the geometric structure in accordance with the input, without exhibiting undesired genus. Furthermore, compared to these two methods, our reconstruction results demonstrate smoother and closer alignment with the ground truth.

Incomplete Point Cloud. The presence of an incomplete point cloud poses a challenge for reconstructing from an unoriented point cloud. In Fig. 13, we present a model with missing points across feature points and lines of the input points. The observations demonstrate that, with the exception of our method, other approaches encounter difficulties in reconstructing the expected sharp features at locations where points are missing. In such cases, existing methods tend to produce smooth transition surfaces. However, our approach is unaffected by this issue due to our dynamic sampling strategy, which introduces supplementary sampling points in proximity to the current surface. This enhances the influence of the loss function on surface optimization, resulting in a reconstruction more aligned

Table 5. Comparing our approach with CAPRI-Net [Yu et al. 2022].

	w/ fine-tuning	NC \uparrow		CD \downarrow		F1 \uparrow	
		mean	std.	mean	std.	mean	std.
CAPRI-Net [Yu et al. 2022]	×	61.79	13.76	92.96	59.29	5.86	8.41
CAPRI-Net [Yu et al. 2022]	✓	92.06	3.82	9.42	3.16	34.47	18.36
Ours	×	98.42	1.10	2.84	1.36	92.79	9.64

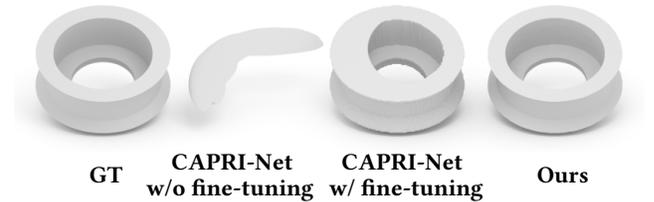


Fig. 10. Visualizing the reconstruction results between CAPRI-Net [Yu et al. 2022] and our NeurCADRecon.

with our loss function settings. Consequently, our method excels in reconstructing sharp feature points and lines even in the absence of certain sampling points.

Comparison with RFEPS. In a recent seminal work on explicit reconstruction, RFEPS [Xu et al. 2022] introduces a method for reconstructing a polygonal surface that incorporates feature lines, utilizing the concept of the restricted power diagram. However, due to the constraints of the restricted power diagram, RFEPS [Xu et al. 2022] faces challenges in reconstructing positions within the CAD model where the dihedral angle is less than $\pi/3$. In contrast, our method is free from this limitation and successfully reconstructs sharp features, as illustrated in Fig. 14. Additionally, RFEPS [Xu et al. 2022] incurs significant time overhead, requiring 3630 milliseconds for a 10K point cloud test, while our method achieves the same task in only 39.58 milliseconds, demonstrating a 92 times improvement in time efficiency.

Comparison with NSH. As previously mentioned, NSH [Wang et al. 2023] encourages the Hessian matrix to be singular, aiming to eliminate ghost geometry while preserving geometric details. This approach is related to, but distinct from our method. Generally, for points near a surface, the Hessian of the SDF aligns with the non-vanishing gradients, with an eigenvalue of 0, rendering the Hessian singular. Only a very limited number of singular points may exist where the Hessian has a non-zero determinant, such as Morse saddle points of the SDF. Thus, NSH [Wang et al. 2023] aims to reduce the number of such singularities without introducing extra smoothness. This is why NSH [Wang et al. 2023] excels at preserving details.

Our method, on the other hand, encourages every point to be a planar point (including feature-line points), except for a limited number of corner points (where k_{Gauss} is significantly different from 0). The introduction of the double-trough function is designed to force the Gaussian curvature to follow a polarization distribution. NeurCADRecon is more effective in recovering sharp feature lines (as seen in the sharp corner in Fig. 15(a)), while NSH is better at reconstructing shapes with rich details (as seen in the eye of the free-form model in Fig. 15(b)). To summarize, NeurCADRecon is tailored

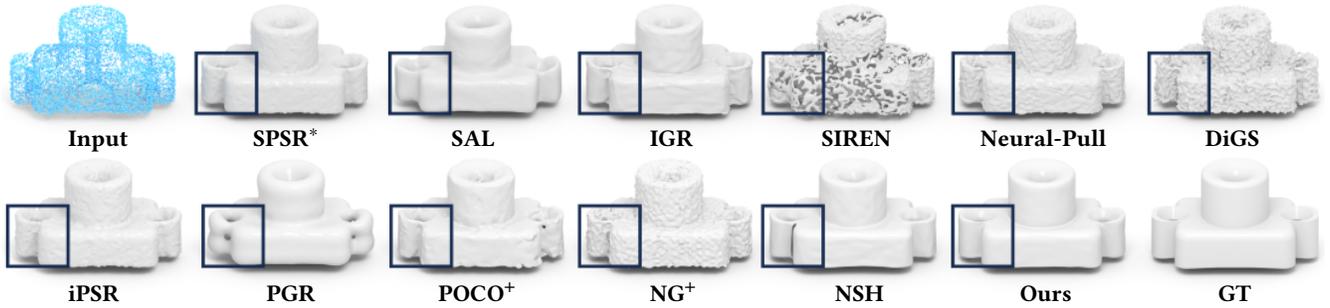


Fig. 11. Evaluate various point surface reconstruction approaches on a point cloud with 0.5% Gaussian noise. Our method stands out as the only approach that effectively recovers a smooth CAD surface even in the presence of input points affected by noise.

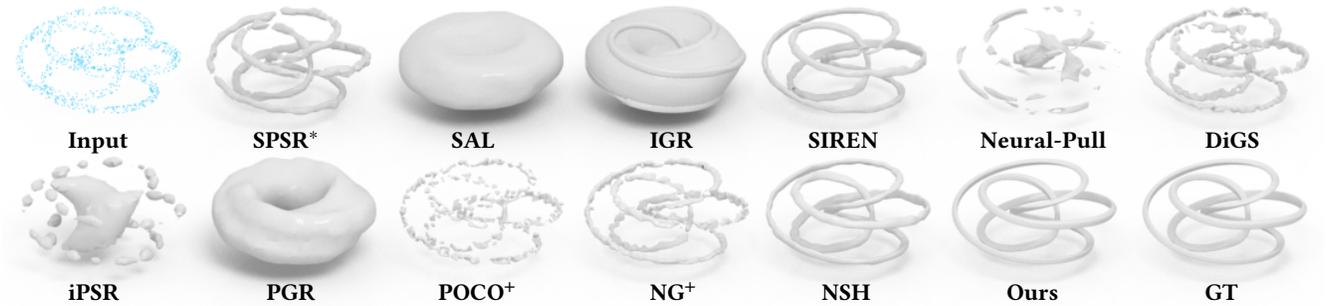


Fig. 12. Experiments are conducted on sparse point clouds containing only 1K points, and our results exhibit a close alignment with the ground truth for the provided input. This comparison highlights the substantial advantage of our algorithm in dealing with sparse raw data.

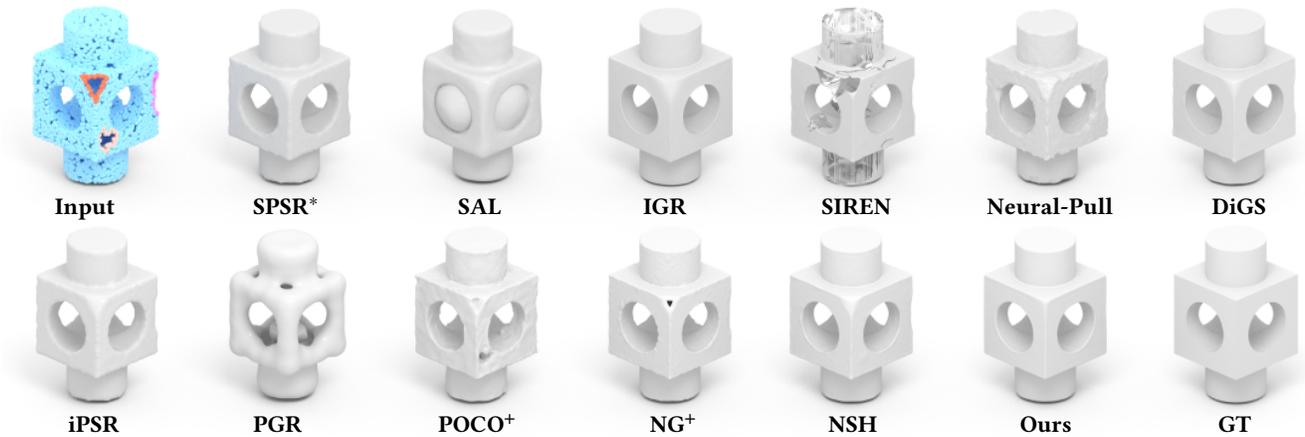


Fig. 13. In a comparison with state-of-the-art methods using an incomplete point cloud as input, characterized by data imperfections across feature points and lines, our NeurCADRecon outperforms other methods in terms of reconstruction accuracy.

for CAD models, whereas NSH [Wang et al. 2023] is intended for non-CAD models.

Additionally, our regularization accommodates the existence of non-90-degree dihedral angles. Although the model in Fig. 15(a) features a non-90-degree dihedral angle, our method can still accurately reconstruct non-90-degree corners. Fundamentally, our double-trough function encourages k_{Gauss} to be 0 or $\pi/2$, but the entire k_{Gauss} distribution must conform to the Gauss-Bonnet theorem [Lee 2018].

Results on Real Scans. In the field of reverse engineering, reconstructing real CAD scans is a pivotal task. To this end, we also evaluate our method’s performance on real scanned CAD models, referenced from Xu et al. [2022]. The point clouds generated by the scanner, specifically captured using a SHINING 3D Einscan SE scanner with an accuracy of 0.1mm, present challenges such as noise and nonuniform density. Benefiting from our Gaussian curvature constraints and dynamic sampling strategy, our method can handle these challenges, preserving feature lines while reconstructing high-fidelity CAD models. For our analysis, the scanned point clouds

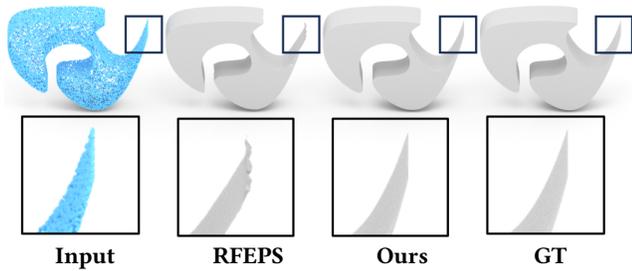


Fig. 14. Visualizing the reconstruction results between RFEPS [Xu et al. 2022] and our NeurCADRecon.

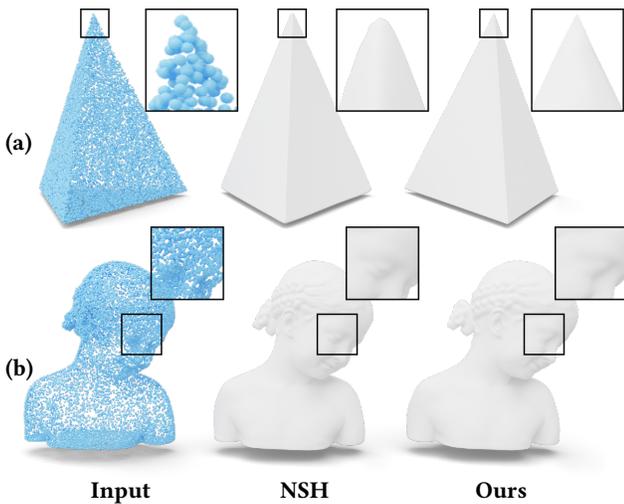


Fig. 15. Visualizing the reconstruction results between NSH [Wang et al. 2023] and our NeurCADRecon.

contain over 100K points, with some including 400K points, so we randomly selected 20K points to serve as input to our network for the fitting process. As depicted in the upper part of Fig. 16, our method demonstrates a remarkable ability to recover fine details and accurately render concave regions of shapes, showcasing its effectiveness in dealing with real-world CAD model reconstructions. In the bottom of Fig. 16, we present the reconstruction results on the input point clouds after introducing 0.5% extra Gaussian noise. Notably, our method demonstrates robustness to noise, consistently yielding faithful reconstructions of CAD models.

4.4 Applications

Developability Enforcement. D-Charts [Julius et al. 2005] paved the way by introducing a straightforward and robust algorithm for mesh segmentation into developable charts. In contrast, our approach focuses on regulating the Gaussian curvature to guide surface deformation towards approximate developability. To ensure the sustained impact of the Gaussian curvature term during optimization, we maintain the annealing factor at 1. In the upper part of Fig. 17 and Fig. 18(a), we showcase qualitative outcomes from our method alongside those from the SOTA methods [Sellán et al.

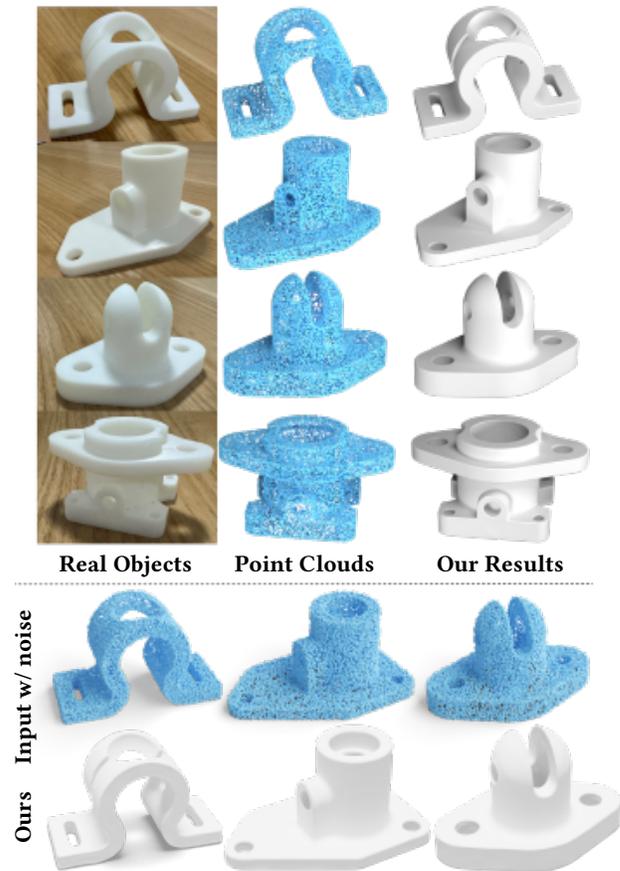


Fig. 16. The reconstruction results of our NeurCADRecon on real scanned point clouds. Upper: Reconstruction results for point clouds scanned by the SHINING 3D Einscan SE scanner. Lower: By adding 0.5% extra Gaussian noise to the input point clouds, our algorithm demonstrates desirable noise resistance.

2020; Stein et al. 2018]. In contrast to Sellán et al. [2020], which often results in an open surface lacking the back side due to its view-dependent nature, our method produces a watertight manifold polygonal surface.

Stein et al. [2018] operates directly on a triangle mesh. Despite its competitive results, the algorithm heavily relies on the mesh tessellation/resolution, and thus cannot consistently produce reliable outputs, as depicted in the upper part of Fig. 17 and 18(a). Our algorithm, independent of mesh tessellation and resolution, can better control the property of developability. Furthermore, for the Armadillo model shown in Fig. 17, our algorithm runs 200 times faster than Stein et al. [2018].

Additionally, as illustrated in the lower part of Fig. 17, it's clear that employing more iterations and a higher weight for λ_{Gauss} facilitates the creation of more developable surfaces. Owing to this distinctive feature, our method is particularly adept at crafting artistic characters by effectively enforcing developability, as exemplified in Fig. 18(b).

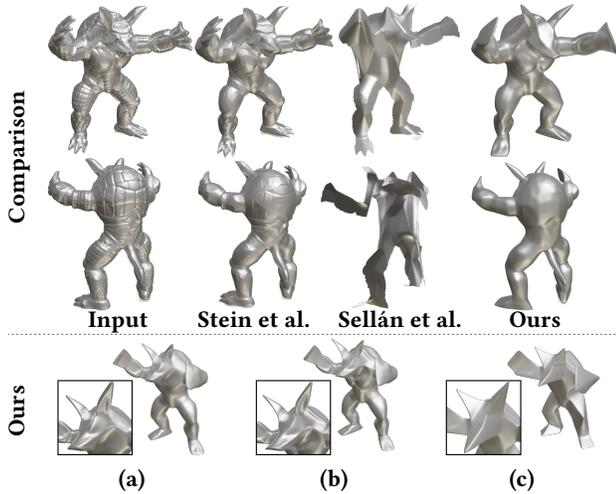


Fig. 17. The upper part of this figure presents the results achieved by our proposed method and those reported in Stein et al. [2018] and Sellán et al. [2020] for the Armadillo model. The lower part of the figure shows the results generated by our method under different parameter settings: (a) $\lambda_{\text{Gauss}} = 3$, #iter 1K, (b) $\lambda_{\text{Gauss}} = 3$, #iter 7K, (c) $\lambda_{\text{Gauss}} = 100$, #iter 7K.

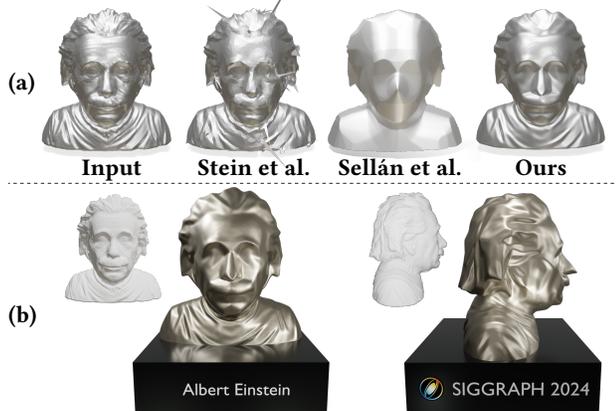


Fig. 18. (a) The results achieved by Stein et al. [2018], Sellán et al. [2020], and our proposed method for the Einstein model. (b) Our approach is well-suited for creating visually appealing artistic characters, thanks to its ability to enforce developability effectively.

Design Recovery. Our algorithm’s capability to accurately capture underlying sharp feature points and lines enables straightforward extraction of a feature-aligned triangle mesh from the SDF, as per Nielson [2004]. Subsequently, this mesh can be decomposed into smooth surface patches, as shown in Fig. 19. Users can then fit a detailed implicit representation to each surface patch, following the methodology outlined by Du et al. [2021]. This functionality proves highly beneficial in secondary design, facilitating a variety of post-edit tasks, such as resizing the CAD model.

5 ABLATION STUDIES

5.1 Isosurface Extraction

In this paper, we utilize the Marching Cubes (MC) algorithm [Lewiner et al. 2003] for isosurface extraction. However, the marching cubes

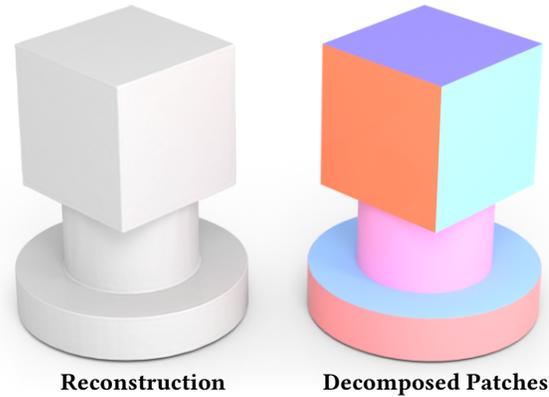


Fig. 19. The reconstructed surface from our method can be decomposed into distinct smooth surface patches along the sharp feature line, significantly simplifying the challenge of recovering the parametric CAD design.

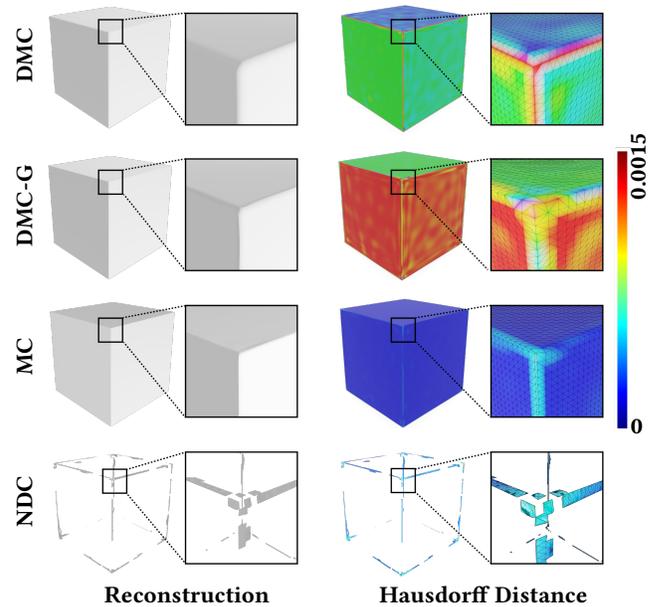


Fig. 20. The zero isosurface extraction results of Neural Dual Contouring (NDC), Marching Cubes (MC), Dual Marching Cubes with gradient (DMC-G), and Dual Marching Cubes without gradient (DMC) for our predicted SDF.

algorithm lacks flexibility, as its vertices consistently align to a fixed lattice. Consequently, the generated meshes may fail to align with non-axis-aligned sharp features. On the other hand, Dual Contouring (DC) [Ju et al. 2002] is popular for its ability to capture sharp features, but it cannot be differentiated. As an improved method, Dual Marching Cubes (DMC) [Nielson 2004] leverages the benefits from both Marching Cubes and Dual Contouring. Recently, Neural Marching Cubes (NMC) [Chen and Zhang 2021] and Neural Dual Contouring (NDC) [Chen et al. 2022] have introduced a data-driven approach to positioning the extracted mesh as a function of the input field.

In this experiment, we apply the SDF fields predicted by our method with the double-trough function to both the MC and DMC

Table 6. Comparison of different smooth energy forms: Dirichlet Energy (E_D), Hessian Energy (E_{H_2}), and L_1 -based Hessian Energy (E_{H_1}). The **best** scores are highlighted in bold with underlining.

	NC \uparrow		CD \downarrow		F1 \uparrow	
	mean	std.	mean	std.	mean	std.
E_D	95.24	2.92	4.11	1.96	80.19	17.82
E_{H_2}	97.54	2.01	3.11	1.61	88.31	14.31
E_{H_1}	97.22	2.25	3.06	1.75	88.59	14.01
Ours	<u>98.21</u>	<u>1.98</u>	<u>3.01</u>	<u>1.51</u>	<u>91.52</u>	<u>13.08</u>

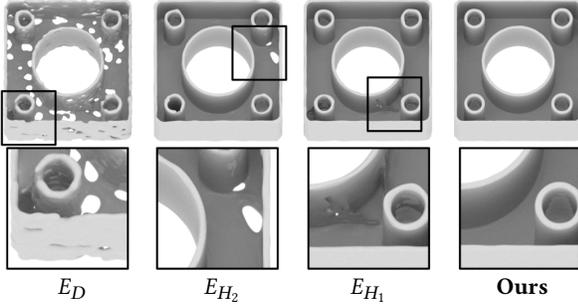


Fig. 21. In a visual comparison of different smooth energy forms, our method demonstrates superiority over other approaches in faithfully recovering the CAD surface without undesirable genus and redundant faces.

algorithms. Notably, DMC is adept at handling scenarios with and without gradient fields. We present the reconstruction results for both cases, where the gradient is calculated using the autograd method in Pytorch. In Fig. 20, we concurrently showcase the four reconstruction outcomes alongside the computed Hausdorff distance between the reconstructed mesh and the ground truth.

Visual inspection in the left segment of Fig. 20 reveals that the polygonal surfaces reconstructed by MC and gradient-based DMC exhibit sharper features at corner positions compared to DMC without gradients. Further scrutiny through the zoomed-in visualization on the right side of Fig. 20 indicates that MC and DMC without gradients struggle to fully capture sharp features at edges and corners. While DMC with gradients can express sharp edges, it still falls short in accurately representing corner shapes. Moreover, a comparison of Hausdorff distances highlights that the reconstruction result of MC is closer to the ground truth. For DMC, both with and without gradients for polygonal surface reconstruction, varying degrees of depressions are observed. In addition, NDC encounters difficulties in accurately extracting the zero isosurface due to divergence issues during optimization. Therefore, we employ the MC algorithm for the extraction of zero isosurfaces in all experiments conducted in this paper.

5.2 Comparison with Other Smoothness Forms

From an algebraic perspective, our Gaussian curvature term can be interpreted as a second-order smooth energy term. Consequently, we compare it with three commonly used smooth energy terms.

Table 7. Ablation studies on the Gaussian curvature constraint term (GCCT). In each column, the **best** scores are highlighted in bold with underlining.

	NC \uparrow		CD \downarrow		F1 \uparrow	
	mean	std.	mean	std.	mean	std.
w/o GCCT	68.29	3.57	9.34	6.84	75.69	18.62
w/ GCCT (Ours)	<u>98.65</u>	<u>1.96</u>	<u>2.19</u>	<u>1.21</u>	<u>91.58</u>	<u>11.36</u>

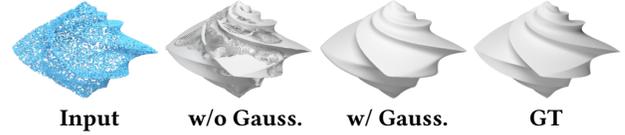


Fig. 22. Reconstruction results are presented both without (w/o Gauss.) and with (w/ Gauss.) the Gaussian curvature term.

They are respectively Dirichlet energy

$$E_D(\mathbf{x}) = \frac{1}{2} \int_{\mathcal{P} \cup \mathcal{Q}} \|\nabla f(\mathbf{x}; \Theta)\|_2^2 dx, \quad (13)$$

Hessian energy

$$E_{H_2}(\mathbf{x}) = \int_{\mathcal{P} \cup \mathcal{Q}} \|H_f(\mathbf{x})\|_2^2 dx, \quad (14)$$

L_1 -based Hessian energy [Zhang et al. 2022]

$$E_{H_1}(\mathbf{x}) = \int_{\mathcal{P} \cup \mathcal{Q}} \|H_f(\mathbf{x})\|_1 dx, \quad (15)$$

where $\|\cdot\|_i$ represents the L_i norm. Note that the Laplacian energy based on the Hessian matrix used by DiGS [Ben-Shabat et al. 2022] is indeed a commonly employed smoothing function, which is also based on SIREN [Sitzmann et al. 2020] like ours. Since we have conducted a detailed comparison with DiGS [Ben-Shabat et al. 2022] in the experimental chapter, we will not delve into the details here.

We randomly selected 100 CAD models from all four datasets for experimental comparison, where each CAD model randomly sampled 10K points as input. Tab. 6 demonstrates that, for the reconstruction of CAD models, our energy function surpasses the other three energy functions in terms of reconstruction accuracy, normal consistency, and Chamfer distance. Moreover, Fig. 21 showcases the superior reconstruction results of our method, highlighting the undesirable genus in the polygonal surface reconstructed by Dirichlet energy and Hessian energy. Additionally, there are redundant faces in the reconstruction result of L_1 -based Hessian energy.

5.3 W/WO Gaussian Curvature Term

To further emphasize the efficacy of our Gaussian curvature loss term in CAD model reconstruction, we conducted a comparative analysis by disabling the Gaussian term.

We randomly selected 100 models for testing and comparison and then set the Gaussian curvature weight term λ_{Gauss} to 0, leaving the other settings unchanged. The compelling performance observed in the quantitative results presented in Tab. 7 underscores the superiority of our method in reconstructing CAD models, providing further evidence of its effectiveness. The qualitative results in Fig. 22

Table 8. A comparative analysis of timing costs and the number of parameters (#Para.) per iteration for IGR [Gropp et al. 2020], SIREN [Sitzmann et al. 2020], DiGS [Ben-Shabat et al. 2022], and NSH [Wang et al. 2023], all executed without the supervision of normals. The timing statistics are meticulously reported in milliseconds (ms).

	IGR	SIREN	DiGS	NSH	Ours
#Para.	1.86M	264.4K	264.4K	264.4K	264.4K
time [ms]	50.73	11.52	36.28	40.10	39.58

Table 9. The runtimes of our method for different input point clouds and resolution of MC [Lewiner et al. 2003], which are reported in milliseconds (ms). We maintained the MC resolution at 256^3 when presenting the runtime efficiency for various input sizes. Similarly, we utilized 10K input points to discuss the runtime efficiency for different MC resolutions.

	Input Size				MC Resolution		
	10K	20K	50K	80K	128^3	256^3	512^3
time [ms]	39.58	46.18	92.35	145.13	9.15	39.58	293.12

indicate that when reconstructing a complex CAD model without utilizing the Gaussian curvature term, the reconstruction results will have an undesirable genus.

5.4 Runtime Performance

We compare IGR [Gropp et al. 2020], SIREN [Sitzmann et al. 2020], DiGS [Ben-Shabat et al. 2022], NSH [Wang et al. 2023], and our method in terms of runtime performance. These statistical insights are derived from our experimental platform, as detailed in Sec. 4.1. For all approaches, we set the batch size to 10K and the number of hidden layers to 4, with each layer containing 256 units. Tab. 8 reports the time costs (in milliseconds) for a single iteration. DiGS [Ben-Shabat et al. 2022], NSH [Wang et al. 2023], and our approach are all based on SIREN [Sitzmann et al. 2020], utilizing identical parameter quantities. In comparison to SIREN [Sitzmann et al. 2020], these three methods demand the estimation of second-order geometric quantities, leading to uniformly higher time consumption than SIREN. IGR runs inefficiently due to a different implementation.

In Table 9, we present the runtime performance of our method across various input sizes of point clouds and different Marching Cubes (MC) [Lewiner et al. 2003] resolutions. The data indicate that as the number of input point clouds and the MC [Lewiner et al. 2003] resolution increase, the time consumption of our method increases relatively slowly. In Fig. 23, we present the reconstruction results of our method across different MC [Lewiner et al. 2003] resolutions.

6 LIMITATION

Our current approach has at least two drawbacks, as seen in Fig. 24. Firstly, when the missing parts of the input point cloud are too large, our approach cannot guarantee the recovery of the actual shape. Secondly, although we use the same parameter to weigh the influence of Gaussian curvature for all experiments in this paper, we notice that there may be some special cases where the parameter needs

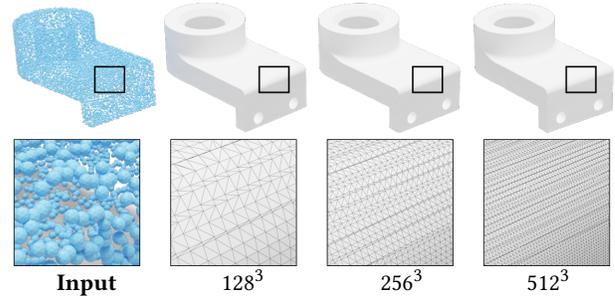


Fig. 23. The reconstruction results of our method across different MC [Lewiner et al. 2003] resolutions, where the magnification ratio is 12 times.

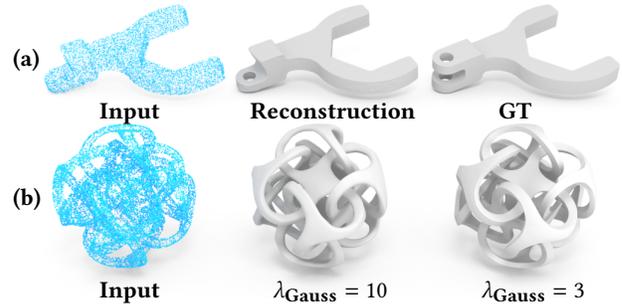


Fig. 24. (a) NeurCADRecon may encounter challenges in cases with a substantial number of missing points. (b) Reconstruction outcomes of a complex model using our method under varying weight conditions.

fine-tuning since the extent to enforce zero Gaussian curvature is related to the inherent geometric complexity.

7 CONCLUSION

In this paper, we introduce NeurCADRecon, a self-supervised approach for neural signed distance function estimation. Our method is designed to work with unoriented point cloud inputs representing CAD models. We leverage prior knowledge that CAD model surfaces are typically composed of piecewise smooth patches, each of which is approximately developable. To achieve this, we minimize the overall absolute Gaussian curvature. To accommodate scenarios where the Gaussian curvature has non-zero values at tip points, we introduce a double-trough curve. Additionally, we propose a dynamic sampling strategy to handle data imperfections. Extensive tests on public datasets demonstrate that NeurCADRecon outperforms existing state-of-the-art methods in reconstructing high-fidelity CAD shapes.

ACKNOWLEDGMENTS

The authors would like to thank the anonymous reviewers for their valuable comments and suggestions. This work is supported by National Key R&D Program of China (2021YFB1715900), National Natural Science Foundation of China (62272277, U23A20312, 62072284) and NSF of Shandong Province (ZR2020MF036).

REFERENCES

- M. Atzmon and Y. Lipman. 2020. SAL: Sign Agnostic Learning of Shapes From Raw Data. In *2020 IEEE/CVF Conference on Computer Vision and Pattern Recognition (CVPR)*. IEEE Computer Society, Los Alamitos, CA, USA, 2562–2571.
- Matan Atzmon and Yaron Lipman. 2021. SALD: Sign Agnostic Learning with Derivatives. In *International Conference on Learning Representations (ICLR)*.
- Yizhak Ben-Shabat, Chamin Hwa Koneputugodage, and Stephen Gould. 2022. DiGS: Divergence guided shape implicit neural representation for unoriented point clouds. In *Proceedings of the IEEE/CVF Conference on Computer Vision and Pattern Recognition (CVPR)*.
- Alexandre Boulch and Renaud Marlet. 2022. POCO: Point Convolution for Surface Reconstruction. In *Proceedings of the IEEE/CVF Conference on Computer Vision and Pattern Recognition (CVPR)*.
- Fatih Calakli and Gabriel Taubin. 2011. SSD: Smooth Signed Distance Surface Reconstruction. *Computer Graphics Forum* 30, 7 (2011), 1993–2002.
- Jonathan C Carr, Richard K Beatson, Jon B Cherrie, Tim J Mitchell, W Richard Fright, Bruce C McCallum, and Tim R Evans. 2001. Reconstruction and representation of 3D objects with radial basis functions. In *Proceedings of the 28th annual conference on Computer graphics and interactive techniques*.
- Rohan Chabra, Jan E Lenssen, Eddy Ilg, Tanner Schmidt, Julian Straub, Steven Lovegrove, and Richard Newcombe. 2020. Deep Local Shapes: Learning local sdf priors for detailed 3d reconstruction. In *Computer Vision—ECCV 2020: 16th European Conference, Glasgow, UK, August 23–28, 2020, Proceedings, Part XXIX 16*. Springer, 608–625.
- Angel X. Chang, Thomas Funkhouser, Leonidas Guibas, Pat Hanrahan, Qixing Huang, Zimo Li, Silvio Savarese, Manolis Savva, Shuran Song, Hao Su, Jianxiong Xiao, Li Yi, and Fisher Yu. 2015. *ShapeNet: An Information-Rich 3D Model Repository*. Technical Report arXiv:1512.03012 [cs.GR].
- Zhiqin Chen, Andrea Tagliasacchi, Thomas Funkhouser, and Hao Zhang. 2022. Neural dual contouring. *ACM Trans. Graph.* 41, 4 (jul 2022). <https://doi.org/10.1145/3528223.3530108>
- Zhiqin Chen and Hao Zhang. 2021. Neural marching cubes. *ACM Trans. Graph.* 40, 6 (dec 2021). <https://doi.org/10.1145/3478513.3480518>
- Xingyi Du, Qingnan Zhou, Nathan Carr, and Tao Ju. 2021. Boundary-sampled halfspaces: a new representation for constructive solid modeling. 40, 4 (jul 2021).
- Philipp Erler, Paul Guerrero, Stefan Ohrhallinger, Niloy J Mitra, and Michael Wimmer. 2020. Points2Surf: learning implicit surfaces from point clouds. In *Proceedings of the European Conference on Computer Vision (ECCV)*.
- Ron Goldman. 2005. Curvature formulas for implicit curves and surfaces. *Computer Aided Geometric Design* 22, 7 (2005), 632–658.
- Amos Gropp, Lior Yariv, Niv Haim, Matan Atzmon, and Yaron Lipman. 2020. Implicit Geometric Regularization for Learning Shapes. In *Proceedings of the International Conference on Machine Learning (ICML)*.
- Fei Hou, Chiyu Wang, Wencheng Wang, Hong Qin, Chen Qian, and Ying He. 2022. Iterative Poisson Surface Reconstruction (IPSR) for Unoriented Points. *ACM Trans. Graph.* 41, 4 (2022), 13 pages.
- Jiahui Huang, Hao-Xiang Chen, and Shi-Min Hu. 2022. A Neural Galerkin Solver for Accurate Surface Reconstruction. *ACM Trans. Graph.* 41, 6 (2022), 16 pages.
- Zhiyang Huang, Nathan Carr, and Tao Ju. 2019. Variational Implicit Point Set Surfaces. *ACM Trans. Graph.* 38, 4 (2019), 13 pages.
- Chiyu Jiang, Avneesh Sud, Ameesh Makadia, Jingwei Huang, Matthias Nießner, Thomas Funkhouser, et al. 2020. Local implicit grid representations for 3d scenes. In *Proceedings of the IEEE/CVF Conference on Computer Vision and Pattern Recognition (CVPR)*.
- Tao Ju, Frank Losasso, Scott Schaefer, and Joe Warren. 2002. Dual Contouring of Hermite Data. *ACM Trans. Graph.* 21, 3 (jul 2002), 339–346.
- Dan Julius, Vladislav Kraevoy, and Alla Sheffer. 2005. D-charts: Quasi-developable mesh segmentation. In *Computer Graphics Forum*, Vol. 24. Citeseer, 581–590.
- Kacper Kania, Maciej Zieba, and Tomasz Kajdanowicz. 2020. UCSG-NET-unsupervised discovering of constructive solid geometry tree. *Advances in Neural Information Processing Systems* 33 (2020), 8776–8786.
- Misha Kazhdan, Ming Chuang, Szymon M. Rusinkiewicz, and Hugues Hoppe. 2020. Poisson Surface Reconstruction with Envelope Constraints. *Computer Graphics Forum* 30, 7 (2020), 1993–2002.
- Michael Kazhdan and Hugues Hoppe. 2013. Screened Poisson surface reconstruction. *ACM Transactions on Graphics (ToG)* 32, 3 (2013), 1–13.
- Michael M. Kazhdan, Matthew Bolitho, and Hugues Hoppe. 2006. Poisson surface reconstruction. In *Eurographics Symposium on Geometry Processing*.
- Diederik P. Kingma and Jimmy Ba. 2014. Adam: A Method for Stochastic Optimization. Johannes Knoblauch. 1913. *Grundlagen der differentialgeometrie*. BG Teubner. 89–94 pages.
- Sebastian Koch, Albert Matveev, Zhongshi Jiang, Francis Williams, Alexey Artemov, Evgeny Burnaev, Marc Alexa, Denis Zorin, and Daniele Panozzo. 2019. ABC: A Big CAD Model Dataset For Geometric Deep Learning. In *Proceedings of the IEEE/CVF Conference on Computer Vision and Pattern Recognition (CVPR)*.
- Ravikrishna Kolluri. 2008. Provably good moving least squares. *ACM Transactions on Algorithms (TALG)* (2008).
- John M. Lee. 2018. *The Gauss–Bonnet Theorem*. Springer International Publishing, Cham, 263–282. https://doi.org/10.1007/978-3-319-91755-9_9
- Thomas Lewiner, Hélio Lopes, Antônio Wilson Vieira, and Geovan Tavares. 2003. Efficient implementation of marching cubes’ cases with topological guarantees. *Journal of Graphics Tools* 8, 2 (2003), 1–15.
- Lingxiao Li, Minhyuk Sung, Anastasia Dubrovina, Li Yi, and Leonidas J Guibas. 2019. Supervised fitting of geometric primitives to 3d point clouds. In *Proceedings of the IEEE/CVF Conference on Computer Vision and Pattern Recognition*. 2652–2660.
- Manyi Li, Falai Chen, Wenping Wang, and Changhe Tu. 2016. Sparse RBF surface representations. *Computer Aided Geometric Design* 48 (2016), 49–59.
- Guying Lin, Lei Yang, Congyi Zhang, Hao Pan, Yuhang Ping, Guodong Wei, Taku Komura, John Keyser, and Wenping Wang. 2023. Patch-Grid: An Efficient and Feature-Preserving Neural Implicit Surface Representation. arXiv:2308.13934 [cs.GR]
- Siyuo Lin, Dong Xiao, Zuoqiang Shi, and Bin Wang. 2022. Surface Reconstruction from Point Clouds without Normals by Parametrizing the Gauss Formula. *ACM Trans. Graph.* 42, 2 (2022), 19 pages.
- Yaron Lipman. 2021. Phase Transitions, Distance Functions, and Implicit Neural Representations. In *Proceedings of the International Conference on Machine Learning (ICML)*.
- Baorui Ma, Zhizhong Han, Yu-Shen Liu, and Matthias Zwicker. 2021. Neural-Pull: Learning Signed Distance Functions from Point Clouds by Learning to Pull Space onto Surfaces. In *Proceedings of the International Conference on Machine Learning (ICML)*.
- Baorui Ma, Liu Yu-Shen, Zwicker Matthias, and Han Zhizhong. 2022. Surface Reconstruction from Point Clouds by Learning Predictive Context Priors. In *Proceedings of the IEEE/CVF Conference on Computer Vision and Pattern Recognition (CVPR)*.
- Lars Mescheder, Michael Oechsle, Michael Niemeyer, Sebastian Nowozin, and Andreas Geiger. 2019. Occupancy Networks: Learning 3D Reconstruction in Function Space. In *Proceedings of the IEEE/CVF Conference on Computer Vision and Pattern Recognition (CVPR)*.
- G.M. Nielson. 2004. Dual marching cubes. In *IEEE Visualization 2004*. 489–496. <https://doi.org/10.1109/VISUAL.2004.28>
- Yutaka Ohtake, Alexander G. Belyaev, Marc Alexa, Greg Turk, and Hans-Peter Seidel. 2003. Multi-level partition of unity implicits. *ACM SIGGRAPH 2005 Courses* (2003).
- A Cengiz Öztireli, Gael Guennebaud, and Markus Gross. 2009. Feature preserving point set surfaces based on non-linear kernel regression. In *Computer Graphics Forum*.
- Jeong Joon Park, Peter Florence, Julian Straub, Richard Newcombe, and Steven Lovegrove. 2019. DeepSDF: Learning Continuous Signed Distance Functions for Shape Representation. In *Proceedings of the IEEE/CVF Conference on Computer Vision and Pattern Recognition (CVPR)*.
- Songyou Peng, Chiyu "Max" Jiang, and Yiyi Liao. 2021. Shape As Points: A Differentiable Poisson Solver. In *Advances in Neural Information Processing Systems (NeurIPS)*.
- Songyou Peng, Michael Niemeyer, Lars Mescheder, Marc Pollefeys, and Andreas Geiger. 2020. Convolutional Occupancy Networks. In *Computer Vision – ECCV 2020: 16th European Conference, Glasgow, UK, August 23–28, 2020, Proceedings, Part III* (Glasgow, United Kingdom). Springer-Verlag, Berlin, Heidelberg, 523–540.
- C. Schroers, S. Setzer, and J. Weickert. 2014. A Variational Taxonomy for Surface Reconstruction from Oriented Points. *Computer Graphics Forum* 33, 5 (2014), 195–204.
- Silvia Sellán, Noam Aigerman, and Alec Jacobson. 2020. Developability of Heightfields via Rank Minimization. *ACM Trans. Graph.* 39, 4 (aug 2020).
- Gopal Sharma, Rishabh Goyal, Difan Liu, Evangelos Kalogerakis, and Subhansu Maji. 2018. CSGNet: Neural Shape Parser for Constructive Solid Geometry. In *The IEEE Conference on Computer Vision and Pattern Recognition (CVPR)*.
- Gopal Sharma, Difan Liu, Subhansu Maji, Evangelos Kalogerakis, Siddhartha Chaudhuri, and Radomír Měch. 2020. ParSeNet: A parametric surface fitting network for 3d point clouds. In *Computer Vision—ECCV 2020: 16th European Conference, Glasgow, UK, August 23–28, 2020, Proceedings, Part VII 16*. Springer, 261–276.
- Chen Shen, James F. O’Brien, and Jonathan R. Shewchuk. 2004. Interpolating and Approximating Implicit Surfaces from Polygon Soup. In *ACM SIGGRAPH 2004 Papers*.
- Vincent Sitzmann, Julien N.P. Martel, Alexander W. Bergman, David B. Lindell, and Gordon Wetzstein. 2020. Implicit Neural Representations with Periodic Activation Functions. In *Advances in Neural Information Processing Systems (NeurIPS)*.
- Michael David Spivak. 1975. A comprehensive introduction to differential geometry, Vol. 3. 204.
- Oded Stein, Eitan Grinspun, and Keenan Crane. 2018. Developability of Triangle Meshes. *ACM Trans. Graph.* 37, 4 (jul 2018).
- Jiapeng Tang, Jiabao Lei, Dan Xu, Feiying Ma, Kui Jia, and Lei Zhang. 2021b. SA-ConvONet: Sign-Agnostic Optimization of Convolutional Occupancy Networks. In *Proceedings of the IEEE/CVF International Conference on Computer Vision*.
- Jia-Heng Tang, Weikai Chen, jie Yang, Bo Wang, Songrun Liu, Bo Yang, and Lin Gao. 2021a. OctField: Hierarchical Implicit Functions for 3D Modeling. In *Advances in Neural Information Processing Systems (NeurIPS)*.
- Mikaela Angelina Uy, Yen-Yu Chang, Minhyuk Sung, Purvi Goel, J. Lambourne, Tolga Birdal, and Leonidas J. Guibas. 2021. Point2Cyl: Reverse Engineering 3D Objects

- from Point Clouds to Extrusion Cylinders. *2022 IEEE/CVF Conference on Computer Vision and Pattern Recognition (CVPR)* (2021), 11840–11850.
- Peng-Shuai Wang, Yang Liu, and Xin Tong. 2022a. Dual Octree Graph Networks for Learning Adaptive Volumetric Shape Representations. *ACM Trans. Graph.* 41, 4 (2022), 15 pages.
- Yifan Wang, Lukas Rahmann, and Olga Sorkine-Hornung. 2022b. Geometry-consistent neural shape representation with implicit displacement fields. In *The Tenth International Conference on Learning Representations*. OpenReview.
- Yifan Wang, Shihao Wu, Cengiz Oztireli, and Olga Sorkine-Hornung. 2021. Iso-points: Optimizing neural implicit surfaces with hybrid representations. In *Proceedings of the IEEE/CVF Conference on Computer Vision and Pattern Recognition*. 374–383.
- Zixiong Wang, Yunxiao Zhang, Rui Xu, Fan Zhang, Peng-Shuai Wang, Shuangmin Chen, Shiqing Xin, Wenping Wang, and Changhe Tu. 2023. Neural-Singular-Hessian: Implicit Neural Representation of Unoriented Point Clouds by Enforcing Singular Hessian. *ACM Trans. Graph.* 42, 6 (dec 2023).
- Karl DD Willis, Yewen Pu, Jieliang Luo, Hang Chu, Tao Du, Joseph G Lambourne, Armando Solar-Lezama, and Wojciech Matusik. 2021. Fusion 360 gallery: A dataset and environment for programmatic cad construction from human design sequences. *ACM Transactions on Graphics (TOG)* 40, 4 (2021), 1–24.
- Rundi Wu, Chang Xiao, and Changxi Zheng. 2021. DeepCAD: A deep generative network for computer-aided design models. In *Proceedings of the IEEE/CVF International Conference on Computer Vision*. 6772–6782.
- Rui Xu, Zhiyang Dou, Ningna Wang, Shiqing Xin, Shuangmin Chen, Mingyan Jiang, Xiaohu Guo, Wenping Wang, and Changhe Tu. 2023. Globally consistent normal orientation for point clouds by regularizing the winding-number field. *ACM Transactions on Graphics (TOG)* 42, 4 (2023), 1–15.
- Rui Xu, Zixiong Wang, Zhiyang Dou, Chen Zong, Shiqing Xin, Mingyan Jiang, Tao Ju, and Changhe Tu. 2022. RFEPS: Reconstructing Feature-line Equipped Polygonal Surface. *ACM Transactions on Graphics (TOG)* (2022), 15 pages. <https://doi.org/10.1145/3550454.3555443>
- Fenggen Yu, Zhiqin Chen, Manyi Li, Aditya Sanghi, Hooman Shayani, Ali Mahdavi-Amiri, and Hao Zhang. 2022. CAPRI-Net: learning compact CAD shapes with adaptive primitive assembly. In *Proceedings of the IEEE/CVF Conference on Computer Vision and Pattern Recognition*. 11768–11778.
- Jingyang Zhang, Yao Yao, Shiwei Li, Tian Fang, David McKinnon, Yanghai Tsin, and Long Quan. 2022. Critical regularizations for neural surface reconstruction in the wild. In *Proceedings of the IEEE/CVF Conference on Computer Vision and Pattern Recognition*. 6270–6279.
- Junsheng Zhou, Baorui Ma, Liu Yu-Shen, Fang Yi, and Han Zhizhong. 2022. Learning Consistency-Aware Unsigned Distance Functions Progressively from Raw Point Clouds. In *Advances in Neural Information Processing Systems (NeurIPS)*.